2021-08-07

ESTIMATION OF IONOSPHERE VTEC USING MULTIVARIATE QUADRATIC MODEL OVER BAHIR DAR, ETHIOPIA IN THE YEAR 2010-2014

Gezehagn, Kasech

http://ir.bdu.edu.et/handle/123456789/12317

ESTIMATION OF IONOSPHERE VTEC USING MULTIVARIATE QUADRATIC MODEL OVER BAHIR DAR, ETHIOPIA IN THE YEAR 2010-2014

SUBMITTED IN PARTIAL FULFILLMENT OF THE
REQUIREMENTS FOR THE DEGREE OF
MASTER OF SCIENCE IN PHYSICS
AT
BAHIR DAR UNIVERSITY

BY
Kasech Gezehagn

BAHIR DAR, UNIVERSITY
BAHIR DAR, ETHIOPIA
JULY, 2021

BAHIR DAR, UNIVERSITY
COLLEGE OF SCIENCE
DEPARTMENT OF PHYSICS

The undersigned hereby certify that they have read and recommend to the Faculty of Graduate Studies for acceptance a thesis entitled "**ESTIMATION OF IONOSPHERE VTEC USING MULTIVARIATE QUADRATIC MODEL OVER BAHIR DAR, ETHIOPIA IN THE YEAR 2010-2014**" by **Kasech Gezehagn** in partial fulfillment of the requirements for the degree of **Master of Science in Physics (Space Physics)**.

Dated: July, 2021

Advisor: ____________________
Dr. Tsegaye Kassa

External Examiner: ____________________
Dr. Epherem Beshir

Internal Examiner: ____________________
Dr. Melesew Nigusie

____
Dr. Raju P.(Chairman)

BAHIR DAR, UNIVERSITY

Date: **July, 2021**

Author: **Kasech Gezehagn**
Title: **ESTIMATION OF IONOSPHERE VTEC USING MULTIVARIATE QUADRATIC MODEL OVER BAHIR DAR, ETHIOPIA IN THE YEAR 2010-2014**
Department: **Physics**
Degree: **M.Sc.** Convocation: **July** Year: **2021**

Permission is herewith granted to Bahir Dar, University to circulate and to have copied for non-commercial purposes, at its discretion, the above title upon the request of individuals or institutions.

Signature of Author

Dedication

This M.Sc. research work is dedicated to my Family.

Table of Contents

List of Figures

Acknowledgements

I would like to thank all my family members for their financial support, love, and encouragement on these thesis work. I would like to express my deepest gratitude and appreciation to my advisor Dr. Tsegaye Kassa for his absolute effort in advising me to conduct my thesis on this title, guidance and encouragement as well as critical comments and ideas starting from the title selection and modification up to the completion of this study. Also, my gratitude goes to my M.sc instructor Dr.Ambelu Tebabal for teaching me and his encouragement. Furthermore, I would like to extend my gratitude to my friend Kalkidan Tewodros and Amen Getent for being with me all the time, giving suggestions and other supports. I extend my sincere gratitude to my classmates for sharing their ideas and suggestions. I really give great respect and credit to everyone who has involved in my thesis work.

Kasech Gezahegn
Bahirdar, Ethiopia
July, 2021.

Abstract

The ionosphere, also known as the ionized part of the upper atmosphere, is believed to vary as a function of different parameters such as solar and geomagnetic activities. One of the peculiar parameters that describes the variability of the ionosphere is its total electron content (TEC). This thesis focuses on modeling and predicting the variability of the daily and hourly vTEC as a function of F10.7 flux and storm time index (Dst) using multivariate quadratic modeling over Bahir Dar, Ethiopia. The analysis was done for 2010-2014 vTEC in both short-and long-term data set. From the modeling, we could infer both the linear and non-linear trends of the TEC as a function of F10.7 and Dst. The previews studies have reported both linear and non-linear trends of TEC variation. It means that there is no conclusive report on linear or non-linear dominancy of TEC variation with respect to solar and geomagnetic indices. We have also predicted the daily vTEC for each year under consideration. Thus, the analysis depicted that such a mixed trend of the vTEC variation is persistently occurring in both modeling and prediction aspects of the work. The deviation between the modeled vTEC and the observation has a clear daily and seasonal variations. Specifically, we could observe high deviation during equinox than solstice seasons. Both the short-term and long-term analysis of the modeling depicted that the linear variation of vTEC as a function of F10.7 and Dst is more dominant than the non-linear variation. We have observed that on average, 70% of the variation of vTEC could be explained by the proposed multivariate quadratic model.
Keywords: ionospheric vTEC, ionospheric variability, ionospheric modeling, ionospheric prediction.

Chapter 1

Introduction

1.1 Background of the study

Ionosphere, which can be defined as the ionized part of the upper Earths atmosphere where sufficient ionization can exist to affect the propagation of radio waves that extends from about 60 km to 1000 km (Davies, 1990). Solar radiation such as extreme ultra-violate (EUV) and X-ray radiation is the primary cause of ionization in the ionosphere. The Suns high-energy X-rays and ultraviolet (UV) radiation interfere continuously with gas molecules and atoms in the upper atmosphere of the Earth (Rees, 1989). The ionosphere is an open system which pairs strongly with the thermosphere and the magnetosphere. The ionosphere is conventionally described in terms of three principal regions, the D, E and F regions. Subdivisions of these regions may exist under certain conditions, these are F_1 and F_2 layers during nighttime.

The ionosphere is significantly varies due to altitude, latitude, longitude, season, solar cycle and geomagnetic activity. This variability can be traced from observations and empirical/physical models. The response to solar activity is mediated by two independent but distinct mechanisms. First, when the sun is active, ionizing radiation is more powerful, resulting in typically larger electron concentrations; second, when the sun is active, the temperature of the neutral upper atmosphere rises, causing ionization redistribution, with peak concentration occurring at higher altitudes especially in the case of the *F* regions (Haigh, 2007; Tinsley, 2003). We commonly use ionospheric total electron content (TEC) and electron density to extract this variability. TEC has been studied and modeled extensively for both scientific and practical purposes in the ionosphere. The importance of the TEC arises from the fact that trans-ionospheric radio signals utilized by the Global Navigation Satellite Systems (GNSS) can have significant range errors, which are proportional to the integral of the electron density along the ray path, proportional to slant total electron content(sTEC). Different ionospheric models have been proposed for ionospheric TEC variability and are formulated by considering solar, geomagnetic and periodic components (Forbes et al., 2000; Balan et al., 1993; Bilitza et al., 2011; Chen et al., 2008; Kassa, 2017; Gao et al., 2002).

Forbes et al. (2000) have formulated an empirical ionospheric model by considering the solar F10.7 index. The solar activity and seasonal components are identified by these investigators as prime contributors to F-region ionospheric variability. For the first time, Afraimovich et al. (2006) offered a novel strategy for analyzing and better comprehending the Sun-Earth relationships and the intension of demonstrating the relation between global TEC and solar activity component, F10.7 index. The global electron content (GEC), which is equal to the entire amount of electrons in the near-Earth space environment at the GPS orbital altitude of around 20,200 km, is the focus of this technique. The fundamental benefit of this technique is that it allows for the disappearance of local ionosphere parameters and the determination of the dynamics of global characteristics. They found that linear dependence is a good approximation for Global Electron Content (GEC) and F10.7 series regression (Gorney, 1990). However, global TEC models do not take into account local characteristics or seasonal variations, which is a drawback (Guo et al., 2007; Hedin, 1984).

In AraujoPradere et al. (2005) and Zhao et al. (2005) it was reported that the variability of the ionosphere increases with geomagnetic activity at all latitudes. The ionosphere is disrupted when there are large spikes and/or decreases in electron concentrations compared to typical levels. An ionospheric storm is a term used to describe the ionosphere's significantly disrupted behavior. It has benefited from decades of research into the description and prediction of ionospheric storm characteristics. Yu et al. (2009) have studied the climatological variations of ionospheric TEC with a new perturbation index (σ) as a function of the solar F10.7 and geomagnetic Ap indices. Accordingly, the global perturbation index correlated well with F10.7 and Ap indices. Similarly, Lean et al. (2011), Li (2013) and Rishbeth (1993) the different factors affecting the TEC climatological variations at different latitudes have been investigated using Global Ionospheric Map (GIM)-TEC data based linear time series TEC model. These models were not evaluated with the standard ionospheric empirical models. The GIM model TEC may not be appropriate for characterizing low-latitude ionospheric variations (Li, 2013).

A few ionospheric models have been built to fulfill the needs of ionospheric physics research and application in GNSS locating with empirical models such as International Reference Ionosphere (IRI) and NeQuick estimations over equatorial and low latitude regions across the India (Bilitza et al., 2011; Kumar et al., 2012; Nava et al., 2008). Many researchers have looked into the accuracy of these models in different parts of the world during different periods of solar and geomagnetic activity. IRI model is generated by the worldwide network of ionosondes, the power full incoherent scatter radars, topside sounders, and in situ instruments flown on many satellites and rockets. IRI-2016 is the latest version for IRI model, which includes several height profiles for a group of plasma parameters such as plasma density, plasma temperatures of electron and ion composition. In this model, the F layer region peak parameter is estimated by URSI (Szuszczewicz et al., 1998) or Consultative Committee for International Radio

(CCIR) 1966 (CCIR , 1967) model. NeQuick model is used to correct ionospheric delays for the Galileo satellite system. It is a 3D ionospheric model, in which can be used to derive TEC along the arbitrary ray from receiver to satellite. In this model ionosphere that generates profiles of electron densities based on parameters extracted from ionograms, that act as anchor points (Hochegger et al., 2000). Consequently, concert climatological improvements in the global empirical models have been achieved with these research findings. More specifically, attempts have also made by numerous researchers to conduct comparative studies between GPS TEC and IRI based TEC over equatorial and low latitude African and American longitudes (Akala et al., 2015; Okoh et al., 2015). They have figured out the drawbacks of IRI model predictions specifically during early morning and post-sunset hours for both solar minimum and maximum conditions.

In this work we have investigated the low latitude ionospheric vTEC variations using multivariate quadratic vTEC model by incorporating two forms of variations named as solar activity (F10.7) and geomagnetic activity (Dst) variations simultaneously. The validation of the multivariate quadratic model is done by comparing the model vTEC with GPS-vTEC. Besides, to demonstrate the accuracy of the proposed model, we have compared it with IRI-2016 ionospheric model. The model parameters are estimated over Bahir Dar, BDMT (geographic $11.60^0N, 37.38^0E$), for the year 2010 to 2014. Consequently, forecasting/prediction of the daily, hourly and long-term vTEC has done over Bahir Dar, Ethiopia ionosphere.

1.2 Statement of the problem

The variation of TEC with respect to solar and geomagnetic indices have been studied by different scholars. This variation is expected to have both linear and non-linear trends. Lei et al. (2005) and liu et al. (2007) reported that the variation of the ionosphere(vTEC) in relation with solar and geomagnetic activities is complicated. Balan et al. (1993) and Kane (1992) reported that the relationship is roughly linear.

According to the above reports, the linearity is characterized by segmented linear. The non linear relationship is also reported by Chen et al. (2008). Kassa (2017) have also confirmed the non linear dominance of the variation as that of Chen et al. (2008). Thus we came to learn that there is no conclusive result on the dominance's of the linear and non linear variation of vTEC as a function of solar and geomagnetic indices.

Besides, as far as our literature knowledge is concerned, there are no reports in Africa in general and in Ethiopia in particular which have been investigated the effect of solar and geomagnetic activities on vTEC using multivariate quadratic modeling. Therefore, we have intended to further deal with the investigation of linear or non-linear variation of vTEC as a function of solar (F10.7) and geomagnetic (Dst) indices using multivariate quadratic modeling. In our case, both short and long-term analysis was treated over Bahir Dar, Ethiopia ionosphere in the year 2010 to 2014.

1.3 Objectives of the study

General objective

The main objective for this thesis is to model and predict ionospheric variation over Bahir Dar, Ethiopia in temporal aspects.

Specific objectives

The specific objectives of this thesis are;

- To Estimate vTEC using solar and geomagnetic indices.
- To predict vTEC from estimate polynomial coefficients

1.4 Thesis Organization

This thesis consists of six chapters. The first chapter shows the introduction of the thesis. The second chapter focuses an overview of the Sun and the Earths neutral atmosphere in detail and the third chapter is about the Earths ionosphere, the formation of the ionosphere, the variability and how it affects the propagation of the GPS signals through the ionosphere. The fourth chapter deals with data sources and methods we have applied. The fifth chapter presents the result and discussion and the last chapter summarizes the conclusion and recommendation of the thesis.

Chapter 2

The Sun and the Earth's neutral atmosphere

2.1 The Sun

The Sun like all stars is a huge ball of extremely hot, mostly ionized gas that shines under its own power and the biggest object in the solar system that emits electromagnetic radiation waves, particles and the ultimate source of energy to our planet. It contains more than 99.8% of the total mass of the Solar System (Jupiter contains most of the rest), which consists of about 78% hydrogen, 20% helium and others consist 2%. The Sun's magnetic field is very strong (by terrestrial standards) and very complicated. Its magnetosphere (also known as the heliosphere) extends well beyond Pluto. In addition to heat and light, the Sun also emits a low density stream of charged particles (mostly electrons and protons) known as the solar wind which propagates throughout the solar system at about 450 km/sec. The solar wind and the much higher energy particles ejected by solar flares can have dramatic effects on the Earth ranging from power line surges to radio interference to the beautiful aurora arboreal. The mean range between sun towards Earth is 1AU (astronomical unit) and it is about 1.5×10^8 km and its the speed is near the speed of light, 3×10^8 m/s. The mass of the Sun is close to $2 \times 10^{30} kg$, and for the given radius of the Sun it leaves the medium mass density at about $1.4 \times 10^3 \ \frac{kg}{m^3}$. The acceleration due to gravity at the solar surface is about $2.7 \times 10^2 \frac{m}{s^2}$ and the escape velocity is 6.2×10^5 m/s (Brekke, 2012). The Sun emits huge amounts of energy and mass (about 4×10^{23} erg/s) that is produced by nuclear fusion reactions (hydrogen converted to helium and gamma rays) in its interior. The diameter of the Sun is 1,391,978 km and its volume are about $1.4 \times 10^{27} m^3$ and its average density is $1428 kg/m^3$. The density within the Sun falls off very rapidly with increasing distance from the center. The central density is about $150 \frac{g}{cm^3}$, and at the surface, it is about $10^{-7} \frac{g}{cm^3}$. The Sun's volume can be divided into its interior and the outer solar atmosphere.

2.1.1 The Sun's interior region

There are three fundamental parts to the Sun's interior, which are the core, radiative zone, and convection zone, as shown in the Fig. 2.1

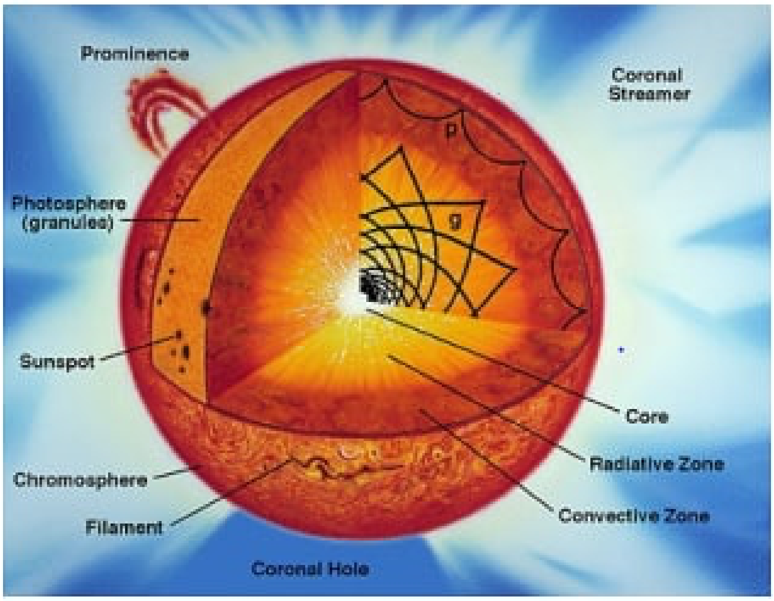

Figure 2.1: Structure of the Sun. (From Encyclopaedia Britannica Inc., 1989)

The Core

The core is the source of the Sun's energy at the center of the Sun in takes place all thermonuclear processes that produce gamma rays and cause the temperature to rise up to $15 \times 10^6 k$ (Gombosi, 1998). The Sun's core is highly dense and is the source of all of its energy. Inside the core, nuclear energy is being released (in ways we will discuss in the Sun of Nuclear Powerhouse). The core is approximately 25% of the size of the solar interior . One half of the solar mass is contained within the core, even though its radius is about one fourth of the sun radius. Thermonuclear processes, such as proton-proton and carbon-cycle chains, will convert protons to helium nuclei at high temperatures. The protonproton chain is seen in the diagram below:

$$^1H +^1 H \rightarrow^2 H + e^+ + v + 0.42MeV$$

$$^1H +^2 H \rightarrow^3 H + \gamma + 5.5MeV$$

$$^1H +^3 H \rightarrow^4 H + 2^1H + 12.8MeV$$

where, e^+, v, γ represent a positron, a neutrino, and a gamma ray quantum, The fusion process that converts four protons into one helium nucleus energy of 24.64MeV $(2 \times 0.42 + 2 \times 5.5 + 12.8)$ is released and the released kinetic energy in this manner will rapidly be converted to local thermal energy that will be transported out of the central regions (Brekke, 2012).

The Radiative zone

Above the core is a region known as the radiative zone named for the primary mode of transporting energy across it. The energy generated by the nuclear reaction in the core must find its way to the surface, where it can be radiated into space. The high energy gamma ray photons are knocked about constantly as they pass through the radiative zone, some are absorbed, some re-emitted, again gradually making their way toward the surface, with the re emitted photons having successively lower energies and longer wavelengths and some are returned to the core (Eby et al., 2005; Eckler, 2011). Full spectrum of radiation from the sun can be obtained after this process. The temperature is around 1.5 million degrees at the radiative zone's outermost limit, and the density is about 0.2 $\frac{g}{cm^3}$. It is less dense than the core. The radiative layer has an insulating effect that helps to maintain the high temperature.

The Convective zone

The convective zone, which stretches from around 70% of the solar radius to the Sun's surface, is at the top of the internal structure. In this region, energy is carried to the surface by a process of convection. Plasma gas heated by the radiative zone underneath rises to the surface in giant convection currents in this zone. If the plasma gas enters the Sun's surface, it cools and sinks back into the Sun to the convection zone's foundation, where it absorbs additional heat from the radiative zone's tip. The solar gas in this area is convectively unstable, in which the buoyancy forces result in up and down the motions.

2.1.2 The Solar atmosphere

The measurable portion of the Sun that covers the observable is called the solar atmosphere. The solar atmosphere is divided into different layers based on the temperature height profile. The three regions in the solar atmosphere are the photosphere, the lower solar atmosphere(chromosphere), and the upper solar atmosphere(corona).

Photosphere

The inner most region in which the visible light (radiation) comes from in this region. The photosphere serves as a boundary between the Sun's interior (opaque region) and overlaying relatively transparent material. The temperature of the photosphere varies between about 6500 K at the bottom and 4000 K at the top and its minimum temperature serves to mark the base of the next layer (Foukal et al., 2004). Solar convective motions continuously churn the outer solar atmosphere. The extra energy is radiated away by bringing hot, high-entropy gas up to the photosphere.

Chromosphere

The chromosphere is located above the photosphere, which is a 2000 km thick gas layer that transports light to the visible spectrum. Is a bright red-colored appears when viewed during a solar eclipse. Its size is certainly larger than that of the photosphere, and the subsequent argument concerning scale height predicts a higher temperature, which ranges from around 4000 K at the bottom to 8000 K at the top.The chromosphere can be observed during short phases of total solar eclipses when the Moon just covers the photosphere. During the total eclipse, the Moon obscures the photosphere and makes way for the reddish chromosphere to be seen. The density decreases continuously by height in the chromosphere. However, the temperature rises until it reaches its lowest point near the top of the photosphere (Brekke, 2012).

Corona

The corona is high temperature portion of the Sun's outer atmosphere beginning slightly above the visible surface Golub (2010). The sun's envelope is made up of electrons and protons, with a minor number of alpha particles and trace convection's of highly ionized heavier elements, and it extends from the transition area to a height of roughly 2000 km to 3000 km (Prlss, 2005).

2.2 Sunspot and solar flare

Sunspots were the first tangible proof of the Sun's fascinating complexity. Magnetic field lines emerge from the photosphere, preventing heat transfer by convection, forming sunspots. Sunspots are cool, dark patches on the Sun's surface that have a lower temperature than the rest of the planeker (Prlss, 2005).

Sunspots and faculae are the most prominent manifestations of the magnetic field in the solar photosphere (Solanki, 2013). The sunspots are colder and darker than surrounding areas of the photosphere. The sunspot cycle, like many other great discoveries, was discovered by accident. Heinrich Schwabe, a German pharmacist and amateur astronomer, was persuaded that a planet within Mercury's orbit, tentatively named Vulcan, must exist. Vulcan would have been difficult to observe due to its near proximity to the Sun, but Schwabe claimed there was a way to detect the planet might be to see it as a dark spot when passing in front of the Sun. Schwabe scanned the Sun and recorded its spots every clear day for 17 years, from 1826 to 1843, in the hopes of finding Vulcan among them. He didn't find the planet but he did observe a constant difference in the number of sunspots over aperiod of approximately 11-year and he published his results in a short article titled "Solar observations during 1843."(Schwabe, 1844) apart from the fact that the number and area of sunspots increase and decrease cyclically every 11 years, any hypothesis attempting to explain solar activity must take into account many other aspects of the sunspot cycle.

The most notable is Hale's discovery in 1908 (Hale, 1908) that sunspots are correlated with strong magnetic fields, that sunspots appear to occur in pairs, that the leading (with respect to the direction of the solar rotation) spots in all pairs have the same polarity and that sunspots tend to occur in pairs on one hemisphere, the trailing spots in the pairs have the opposite polarity, while the polarities are oppositely oriented on the other hemisphere and that the polarities in the two hemispheres reverse in corresponding 11-year sunspot cycles (Hale., 1925). Latter on another scientist Wolf discovered a cycle length which supports the Shewabes finding that is about 11 years (Brekke, 2012). Wolf comes with a quantitative description based on data from 1700 to 1848 with the most popular index of solar activity is based on a count number of sunspots 12 on the solar disk. The fundamental index is the regular reckoned relative Sunspot (Wolf) numbers, which are formulated as follows: (Davies, 1990).

$$R_z = K(10_g + f)$$

Where f is the total number of sunspots whatever the size is, g is the number of sunspot groups, and k is normalization constant for his observation.
When sunspots are plotted according to their latitude and longitude, a very distinct butterfly pattern emerges after each 11-year cycle in Fig. 2.2. This butterfly diagram shows one can also notice that around minima sunspots from both old (at low latitudes) and new cycles(at higher latitudes) coexist.

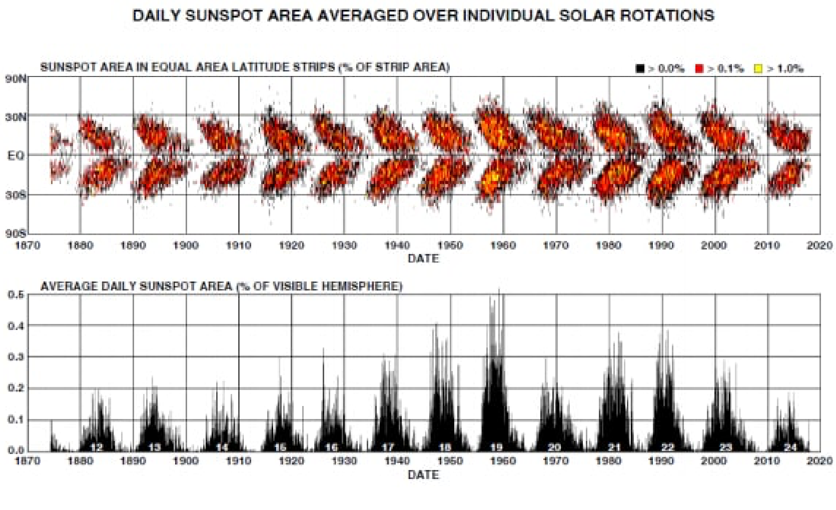

Figure 2.2: Butterfly diagram (top) and average daily sunspot area (bottom). After D. Hathaway (http://solarscience.msfc.nasa.gov).

The solar cycle is the periodic variation in the activity or intensity of the Sun. The solar cycle lasts about eleven years on average, with each cycle beginning with a solar minimum and ending with the next solar minimum. The 11-year variations in solar activity are important sources of decade variations in the solarterrestrial environment. It is well known that the maximum number of sunspots differs during each 11-year cycle. Some cycles show a large number of sunspots, whereas other cycles show few sunspots (Clette et al., 2014). The Sun's magnetic field reverses during each sunspot cycle, so the magnetic field returns to its original orientation after 22 years. This causes the number of sunspots to fluctuate over an 11-year period. The prediction of the magnitude of the 11-year sunspot period is a critical activity for long-term space weather prediction Pesnell (2016) because the maximum number of sunspots is closely linked to solar flares and coronal mass ejections (Tsuneta et al., 1992; Imada et al., 2013). The solar cycles do not have the same number of sunspots at solar maximum that varies from cycle to cycle. The higher numbers of sunspots relate to other significant physical quantities that have a direct effect on the ionosphere and the GPS signals that pass through it sunspots do not become large at a time. Sunspot number data collected prior to the 1700s show epochs in which almost no sunspots were visible on the solar surface. One such epoch, known as the Maunder minimum (see Fig. 2.3) occurred between the years 1642 and 1705, during which the number of sunspots recorded was very low in comparison to later epochs (Hathaway et al., 1994).

The sunspots move from East to West on the solar disk. The effective temperature of a large sunspot is about 4500k which is cooler than the surrounding. The 11-year activity cycle is clearly visible in the space-borne measurements of the total (TSI) and spectral solar irradiance (Solanki, 2013; Ermolli et al., 2013). The present-day TSI change due to the 11-year solar cycle is about 0.1%, while the variability in the UV spectral domain is significantly higher. The arriving charged particles interact with Earths magnetic field and can cause significant changes to the morphology of the ionosphere. A variation of such effect known as the Substorm occurs primarily in

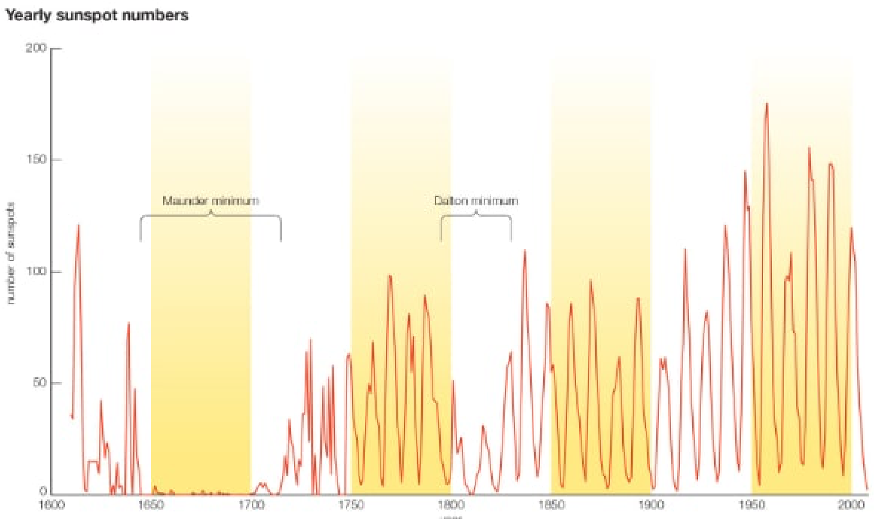

Figure 2.3: Sunspot cycles. Taken from http://solarcyclescience.com/solarcycle.html.

the polar and auroral regions, lasting for several hours (Langley, 2000).

2.3 Solar phenomena

The levels of extreme ultraviolet flux, coronal mass ejections, solar flares and solar winds, which affect the outermost geomagnetic field lines and produce fluctuations and disruptions in the Earth's ionosphere are some of the solar phenomena that are both a function of sunspot counts.

2.3.1 Solar flare

Solar flares are brightening variations that occur suddenly, rapidly, and intensely near sunspots and are caused by powerful solar eruptions that release energetic particles into the atmosphere. The initial instability has been analyzed by considering either a magnetic flux tube or a magnetic arcade and in each case the anchoring or line typing of the potospheric foot points in the solar surface provides a strong stabilizing features that allows magnetic energy to be built up it a stable manner by twisting or hearing motions(into space). The mechanism of solar flares has long been a mystery. Solar flares release X-rays, high-energy particles and Coronal Mass Ejections (CMEs) into interplanetary space in the heliosphere, making them one of the sources of space weather (Schwenn et al., 2005; Fletcher et al., 2011; Liu. et al., 2014; Mstl et al., 2015). Solar flares are the most direct effect of solar activity and they have a significant impact on ionospheric conditions, which can interfere with radio and satellite communications.

2.3.2 Coronal Mass Ejection (CME)

A large eruption of magnetized plasma from the Sun's outer atmosphere (corona) that propagates outward into interplanetary space is known as a coronal mass ejection (CME). CMEs are often associated with flares, but they may also occur without a flare. CMEs were discovered in the early 1970s thanks to observations from spacecraft such as Seventh orbiting Solar Observatory(OSO-7) Thernisien et al. (2011) and Skylab (MacQueen et al., 1994). CME observations have been routine since the Solar Maximum Mission. The frequency of CMEs is often associated with the number of sunspots, but the correlation varies depending on the data used, the concept of a CME and the process used to locate them (Webb, 1994).

2.3.3 Solar wind

Solar wind is the outflow of fully ionized gas from the solar corona on a continuous basis (Parker, 1965). It consists of protons and electrons, with an admixture of a few percent alpha particles and much less abundant heavy ions in different ionization stages and atomic nuclei ejected from the upper atmosphere of the Sun with speeds ranging about 250 km/s to 800 km/s and that also the stream of particles varies in temperature over time. The solar wind has a typical number density of $\approx 10\ cm^{-3}$ and a temperature of $10eV$. These densities and temperatures are much lower than those in the solar corona (≈ 106 cm^{-3} and 102 eV respectively) and higher than those in interstellar space (Kivelson et al., 1995).

2.4 The Earth's neutral atmosphere

Atmosphere is surround Earth and protects us by blocking out dangerous rays (EUV and X-ray) from the Sun. It is a mixture of gases that becomes thinner until it gradually reaches space. The surface of the Earth 78% of the Earths atmosphere is made of the gas Nitrogen (N_2) and 21% is composed of Oxygen (O_2) as its major constituents and lesser amounts around 1% is made up of Argon (Ar), Carbon dioxide, Helium, Hydrogen and Ozone (Jursa, 1985). The atmosphere can be divided into a series of layers, based on the chemical composition, vertical distribution of temperature, or degree of ionization. As regards to its chemical composition, the atmosphere is generally divided into two layers: the homosphere and the heterosphere.

The homosphere is a layer of uniform and relatively well-mixed composition, with respect to the major constituents extending up to about 100 km (Wallace, 1994; Miller , 1979; Iribarne, 2012). The heterosphere is the layer above the homosphere with varying composition. In this layer, molecular diffusion becomes an important process, responsible for the stratification of the gases according to their molecular weight. Positively charged particles and free electrons are a significant part of the air composition within this layer. The outer atmosphere beginning from about 50 miles from the earths surface and extending to space Gases are not evenly mixed but assorted by gravity according to their atomic weight and reaction of the gases with solar radiation. Less than 0.001% of the mass of the earths atmosphere. The density of the atmosphere decreases outward, because of the gravitational attraction of the planet, which pulls the gases and aerosols (microscopic suspended particles of dust, soot, smoke, or chemicals) inward, is greatest close to the surface (Kelley, 2009). There are several ways of classifying the different layers of the atmosphere.

The most common classification is based on the vertical distribution and variations of temperature in the atmosphere. So, based on vertical temperature profile atmospheric layer can be divided in to four. These are Troposphere, Stratosphere, Mesosphere and Thermosphere as shown in the Fig 2.4 below (Hunsucker, 2007; Moldwin , 2008).

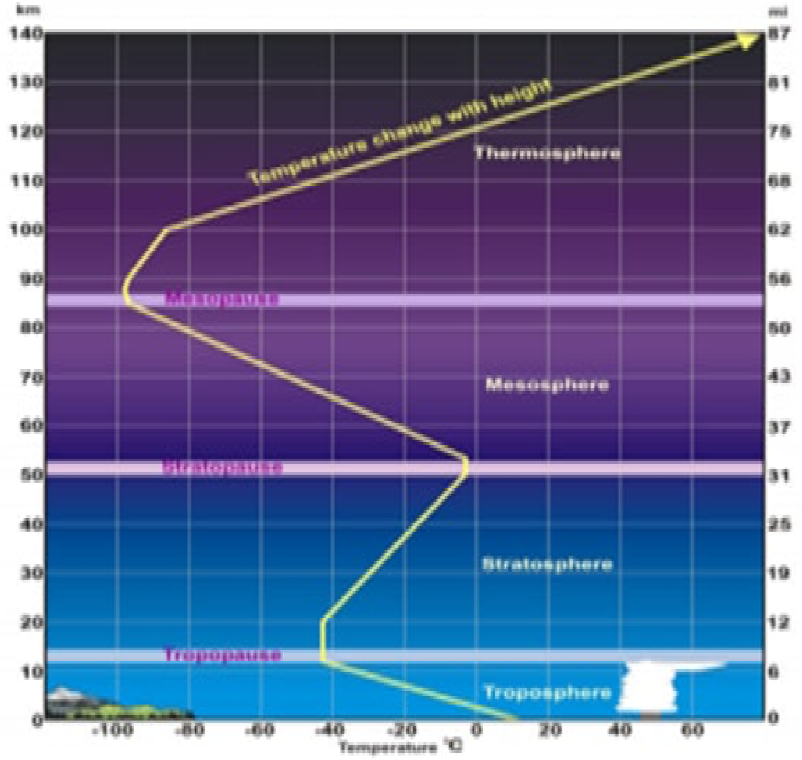

Figure 2.4: The typical profile of neutral atmospheric temperature with various atmospheric layers (*www.srh.NOAA.gov*).

2.4.1 Troposphere

The lowest layer of the atmosphere is the troposphere. It is characterized by a general constant decrease of the temperature with increasing height of about $6.5^oC/km$, on average. Troposphere is mainly heated by the warm ground which both heats the air at the ground level and emits infrared radiation, which is absorbed at greater heights. Because the infrared radiation is emitted out radially, it is distributed to a larger volume with distance and therefore a temperature decrease with height occurs. The troposphere contains about 75% of the total molecular mass of the atmosphere Wallace (1994); Fleagle (2011) and as mentioned before, nearly all the water vapor and aerosols. The upper limit of the troposphere is characterized by a sudden change in the temperature gradient, a level called the *tropopause*, which marks the transition to the stratosphere. The tropopause height is variable and depends on time and place and the tropopause at a height of 10-15 km, and it is a very coldest region with in which the decrease of temperature stops and where a minimum in temperature of about (220^0K) is encountered (Brekke, 2012).

2.4.2 Stratosphere

Above tropopause the temperature again increases with height. This region is the stratosphere. This layer extends from 10km to 50 km. The increasing of temperature in the stratosphere is caused by the presence of ozone (O_3) layer located between 15 and 40 km above ground absorbs a large portion of solar radiation between 200 and 300 nm. The ozone molecules absorb high-energy UV rays from the Sun, which warm the atmosphere at that level. The terrestrial stratosphere is the region between the tropopause, or the end of the troposphere and the level at which the maximum warming due to the presence of ozone takes place and therefore the temperature increases. 90% of the ozone in the Earth's atmosphere lies in the region called the stratosphere which is found between 16 and 48 kilometers above the Earth's surface.

Ozone and oxygen molecules in the stratosphere absorb ultraviolet light from the Sun, providing a shield that prevents this radiation from passing to the Earth's surface. While both oxygen and ozone together absorb 95 to 99.9% of the Sun's ultraviolet radiation, only ozone effectively absorbs the most energetic ultraviolet light, known as UV-C and UV-B, which causes biological damage. The protective role of the ozone layer in the upper atmosphere is so vital that scientists believe life on land probably would not have evolved and could not exist today without it. The upper boundary of stratosphere is the *stratopause*, where the temperature gets a maximum of about 280 K (70C). The altitude of stratopause is not well defined, but it is of the order of 50 km.

2.4.3 Mesosphere

The mesosphere is a layer within the Earth's atmosphere that extends from about 50Km height (above the stratosphere) and about 90 km(below the thermosphere). Where the air masses are relatively mixed together and the temperature decreases with altitude. Atmospheric temperatures reach the lowest average value of around -90^0C in the mesosphere. This is also the layer in which a lot of meteors burn up while entering the Earth's atmosphere. The composition of gases in the atmosphere from the ground to the top of the mesosphere, are almost identical except for water vapor and ozone. A minimum of about 160-180K (about -100^0C) is encountered at a height of 70-90 km. This is the *menopause* and it is the coldest place in the atmosphere. Heat flows towards menopause by conduction from above and is removed by radiation in infrared and visible air glow as well as by eddy transport into the mesosphere.

2.4.4 Theromosphere

Above the menopause the temperature strongly increases with height and the region called the thermosphere. Here solar radiation in the UV band is strongly absorbed due to dissociation of molecules like O_2, N_2, and NO and ionization of atomic oxygen and other molecules and atoms (Brekke, 2012). This leads to the temperature increase in the thermosphere. The maximum temperature, reached at -500 km, varies between about 400^oC and about 2000^0C, depending on the time of day, latitude and solar activity (Iribarne, 2012; Fleagle , 2011). Due to molecular diffusion, a high concentration of light gases can be found in this layer, making the air density very low. In the upper part of the thermosphere the thermal conductivity is so high that this region is kept nearly in an isothermal condition. The thermospheric temperature is of the order of $1000 - 2000K$ and it varies with the time of day and with solar activity. The portion of the thermosphere where charged particles (ions) are abundant is called the ionosphere. These ions result from the removal of electrons from atmospheric gases by solar ultraviolet radiation. The region of the atmosphere above about 80 km is also caused the "ionosphere", since the energetic solar radiation knocks electrons off molecules and atoms, turning them into "ions" with a positive charge.

2.4.5 Exosphere

The exosphere is defined as the region where the mean free path (average distance traveled by a molecule between two collisions) is so great that the lighter particles tend to escape from the atmosphere. The main constituents of this layer are atomic oxygen, ionized oxygen, and hydrogen atoms. This is the true upper limit of the Earth's atmosphere. The exosphere extends from the thermosphere out to space.

Chapter 3

The Earth's Ionosphere

3.1 Introduction

The ionosphere is the partly ionized area of the upper atmosphere of the Earth. This ranges from approximately 60 km to 1000 km. In this region free electrons and ions can exist for a considerable period of time, resulting in the formation of a plasma gas containing charged particles (Schunk, 2009). The main source of the ionization in the ionosphere is the solar radiations such as extreme ultra violate (EUV) and X-ray radiations spectrum are responsible for the ionization process that causes the electrons to break away from the gaseous O, O_2 and N_2 molecules. In addition to photoionization, collision ionization due to particle precipitation from the magnetosphere is another source of ionization in particular in the high latitude region.

The ion composition varies in response to changes in molecular constituents in the neutral atmosphere. NO^+ and O_2^+ are depicted in Fig 3.1. are the dominant ions below 150 km, above which atomic oxygen ions O^+ are the dominant ions are more plentiful. H^+ is a more common ion species above 300 km than either O_2^+ or NO^+. O^+ has the potential to dominate even at distances of $600 km$ and higher. However, magnetosphere and solar conditions can have a significant impact.

Heavy ions will dominate up to $200km$ or more in the aurora area for strong disturbances (Brekke, 2012).

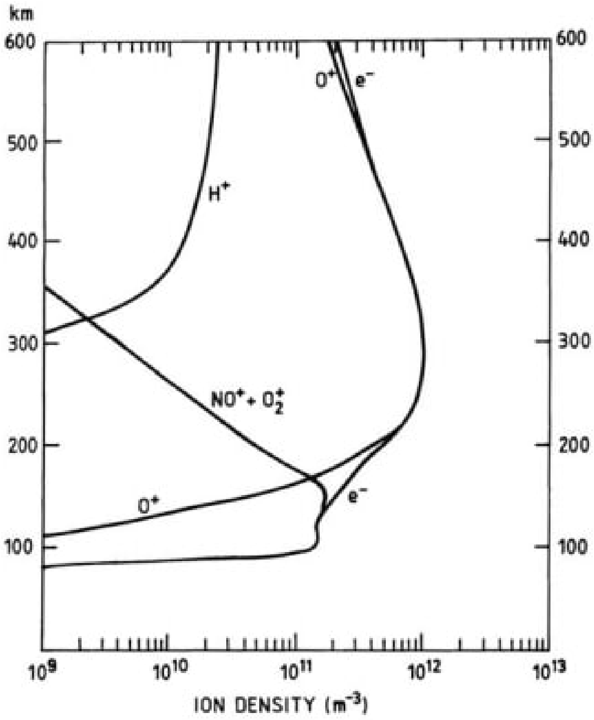

Figure 3.1: Altitude profiles of the most typical ion species in the ionosphere between 100 and 600 km, together with the corresponding electron density profile. (After Richmond, 1987.)

The ionosphere plays a significant role in radio propagation, which is highly variable. Extremely low frequency (ELF=3300 KHz) and very low frequency (VLF=330 KHz) frequencies (Cummer, 2000).

3.2 Formation of the ionosphere

The ionosphere is an open system which pairs strongly with the thermosphere and the magnetosphere. Different photochemical and chemical reactions and dynamical and electrodynamical processes in the exchange of structures and mass, momentum and energy transport in complex ways (Gorney, 1990). The ionosphere is mainly created by the chromosphere and corona of solar XUV emissions. The extent of ionization is determined by temperature.

The majority of the atoms in the plasma remain neutral because the temperature is low, but when exposed to radiation in the form of solar illumination, the atoms absorb this energy and an ionization effect occurs (Hunsucker, 2007). In the ionosphere, the concentration of ions varies with the amount of solar radiation bearing down on Earth. During the day, the ionosphere becomes thick with charged particles, but the density subsides at night when charged particles recombine with electrons that are displaced. The high energy of EUV and X-ray photons from the sun influences atmospheric atoms and molecules. free electrons and positively charged ions are formed as a result of the interaction of solar radiation with atmospheric constituents. The absorption of solar radiation (primarily ultraviolet, extreme ultraviolet, and Xrays) by neutral gases McNamara (1991), the most important of which is atomic oxygen(O, ionized to O^+) at about 60 to 300 km altitude Ratcliffe (1974) causes ionisation (the splitting apart of electrons from atoms and molecules).

3.3 Ionospheric regions

The maximization of ionization activity at various altitudes causes different regions in the ionosphere. The ionospheric regions were divided into three layers based on the mean vertical profile of electron density. The earliest detected was the E layer, so named because of the reflections of electric fields. For alphabetical order we have since got D and F layers below and above the E-layer, respectively. Today it is more common to speak about regions as distinctions between layers are not all that clear, except maybe for some special events in the E-region such as sporadic and aurora E-layers. Before we go into more detail about the different aspects of ionospheric composition, temperature, and dynamics, we will discuss how ionization in the upper atmosphere is produced by solar radiation.

The vertical structure also includes several ionization layers occurring in the D, E, and F layers as shown in the Fig 3.2.

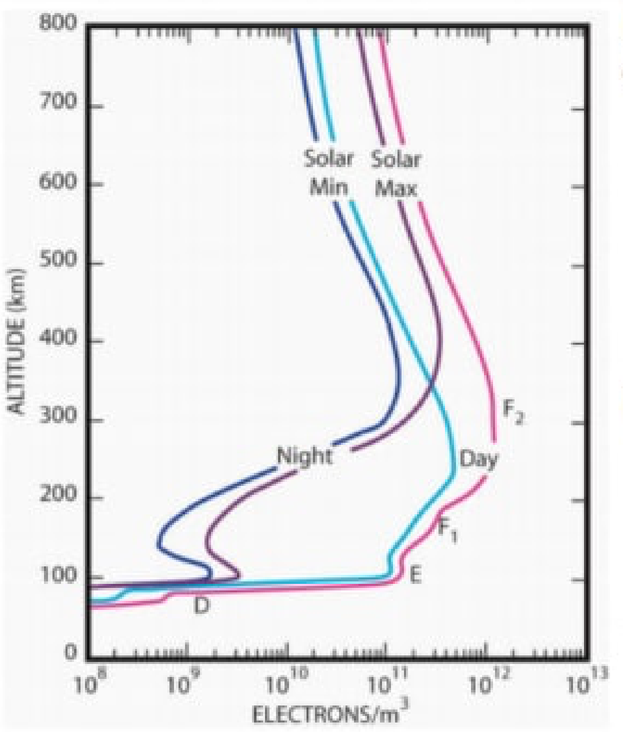

Figure 3.2: The height profile of ionospheric electron density for day and night-time during solar maximum and minimum conditions

3.3.1 D-region

The D region is the lowest at altitudes between 60 to 90km where the atmosphere is comparatively dense. It is produced by hard X-rays from the Sun during the daytime and quickly disappears at night. The D region is very weakly ionized, highly collision, primarily composed of molecular oxygen ions (O_2^+) and nitric oxide ions (NO^+), ionization results mostly from photoionization of NO by Lyman-α radiation

(121.6nm) and a molecular O_2, N_2, and NO. Since the air density is still relatively high at this latitude, the ions and electrons present can easily recombine, resulting in a strong diurnal variation in electron density in the D region (Hunsucker, 2007). During the day, some reflection can be obtained from the D field, but the frequency of radio waves is reduced this is the cause of the marked reduction in the range of radio transmissions in daytime.

3.3.2 E-region

Below the F region is the E layer produced by ionization of molecular and atomic oxygen and molecular nitrogen by soft X-ray and Lyman β radiation (102.6 nm). It ranges from about 90 km to 150 km (McNamara , 1991), and is present throughout the day with a much reduced electron density at night. This layer is present basically by day and decreases by night. Its shape be only a simple in flexion in the profile ,but a valley usually appears thus marking a local maximum. The production processes in the E region are very complex since electrons and ions recombine quite quickly here, ionization levels drop rapidly after sunset and the E layer almost vanishes during the night (Schunk, 2009). An additional feature of this region the appearance of its transient character is called sporadic E layer (Es layer), a thin layer that same times shows large enhancements of electron density and is associated with quasi periodic amplitude scintillation's (Coco et al., 1995).

3.3.3 F-region

The F-layer is the most prominent layer of the ionosphere, containing the majority of the electron content and is ionized by ultraviolet and extreme ultraviolet radiation. This layer extends from about 150 kilometers above the Earth's surface to about 1000km (Rishbeth., 1969). The F region is the most critical layer for long distance communication and it often splits into F_1 and F_2 sub-regions throughout the day.

The F_1 region is located approximately 150 km to 210 km above the Earth's surface, which exists only during daytime and can be distinguishable as an in-flexion in the profile. When it is present, it changes rapidly in a matter of minutes. It is more pronounced during the summer than during the winter months for low solar sunspot numbers and for periods with ionospheric storms. The ionization at this region is caused by the absorption of EUV radiation and by the molecular species (O^+, N_2^+). The electron densities are largely derived from the Sun's zenith angle, which accounts for the day experienced by GPS and the most abundant ion in this area is atomic oxygen (Hunsucker, 2007).

The F_2 region is located approximately 210 km to 1000 km above the Earths surface which contains the maximum of the electron density profile and is predominantly populated with oxygen ions (O^+). The maximum electron density is typically 10^6 electrons per cubic centimeter (Schunk, 2009). The ionization of oxygen and molecular nitrogen by extreme ultraviolet radiation(EUV) is the primary cause of the F2 region. Although it does not disappear during night-time, the electron density during this period decreases by about one order of magnitude. It is also very sensitive to the sunspot cycle. The region below the F2 region (D, E, F1) is referred to as the bottom side of the ionosphere, whereas the region above is referred to as the topside.

3.4 Variability of the ionosphere

The Sun and its activities are the main source of ionization of the ionosphere (Carpenter, 2004). The existence of free electrons and the ionosphere shows a wide range of spatial and temporal variability of electron density, ranging from small fluctuations to large changes. The ionospheric structure and the temporal variation of the Earth-Sun geometry is related to the Earths daily rotation and yearly revolution and the electron density distribution varies considerably with time (diurnally, seasonally), space (geographic location), Suns activity (sunspot cycle) and with other solar-related ionospheric and geomagnetic disturbances.

3.4.1 Diurnal variation

Due to the earth rotation, the relative position of the Sun and Earth changes with time , following a daily cycle. As the Earth rotates with respect to the Sun, the intensity of the solar radiation increases and the ionization also increases to a maximum at around noon. Because of the Earth's rotation around the Sun, the density of electrons varies from day to night (Chapman, 1931). The Sun's large EUV and X-ray radiations cause a higher electron density during the day than at night, when photo-ionization is absent (Chapman, 1931; Rishbeth., 1969; Kelley, 2009).

3.4.2 Seasonal variation

Due to shifting orientation of the Sun with respect to the Earths axis, high electron density values are usually seen during the equinoctial months (March and September) and in summer, although low values are seen in winter (Chapman, 1931). As the Earth revolves around the Sun, a seasonal cycle is generated and determined by which hemisphere the Sun is overhead. It is summer on the hemisphere where the Sun is overhead and winter on the other hemisphere. During solar cycle 23 Lee et al. (2004) analyzed the seasonal anomaly, which occurs mostly at mid latitudes and is more apparent in the northern hemisphere than in the southern hemisphere. Specifically, the summer-to-winter neutral circulation results in an increase in the O/N_2 ratio in the winter hemisphere and a decrease in the summer hemisphere. Due to the relative rise in the production rate and decrease in the loss rate, the increased O and decreased N_2 densities in winter act to enhance the O^+ densities (liu et al., 2007). This effect is more than enough to compensate for the increased solar zenith angle's tendency to lower O^+ densities. The Sun is overhead at the equator around the time of the equinoxes. Seasonal variation influences animal anatomy, such as body size or fat layers (Heldmaier et al., 1981; Aars , 2002), physiology, such as hormone secretion, and human actions (Romero, 2002). Changes in photo period can cause seasonal adaptations, which are mediated by neuroendocrinology (Goldman, 2001).

3.4.3 Latitudinal variations

The diurnal and seasonal behaviors observed the Suns position relative to the atmosphere plays significant role in latitudinal variation in the ionospheric electron density because the solar zenith angle (χ) measured from the observers local vertical to the Sun determines the intensity of ionization. Over the equator the ionospheric densities are expected to be higher compared to other geographic locations. Solar radiation enters the atmosphere at an oblique angle as latitude increases on either side of the geographic equator, resulting in lower ionospheric concentrations.

3.4.4 Solar cycle variation

Solar activity fluctuates during an 11-year cycle, affecting modern life in a variety of ways. Increased solar activity results in an increase in the Sun's extreme ultraviolet and X-ray radiation, which have significant impacts in the upper atmosphere. At many altitudes, the related atmospheric heating raises the temperature and density of the atmosphere (Pulkkinen, 2007). Ultimately, TEC changes with solar activity, with the highest levels occurring during periods of maximum solar activity and the lowest values occurring during periods of solar minimum (Habarulema, 2010). The sunspot number is one of the most commonly used indicators of solar activity. This periodicity can also be detected studying the variability of the electron density.

3.4.5 Geomagnetic activity

Geomagnetic activity, like sunspot area, radio flux, and flares and CMEs, has a solar cycle reliance, but it's more complex. There are a number of indices of geomagnetic activity; most measure rapid (hour-to-hour) changes in the strength and/or direction of Earths magnetic field from small networks of ground-based observatories. The majority of geomagnetic activity indices use tiny networks of ground-based observatories to measure rapid (hour-to-hour) variations in the strength and/or direction of Earth's magnetic field. The ap index is a three-hour interval measurement of the range of variability in the geomagnetic field (in 2 nT units) from a network of roughly high-latitude stations (Svalgaard et al., 2004). Another frequently used index is Dst, disturbance storm time, derived from measurements obtained at four equatorial stations, since 1957.

3.5 Absorption of Ionization radiation

Ionization of greenhouse gases such as N^2, O^2, and O creates the ionosphere, and the requisite energy comes from solar radiation in the extreme ultraviolet (EUV) and X-ray sections of the spectrum (Lilensten et al., 2008). The high energy from the Sun and from cosmic rays, the atoms in this area have been stripped of one or more of their electrons or ionized and are therefore positively charged. The ionized electrons behave as free particles (Gillaspy, 2001). Most of the electrical activity in the ionosphere is produced by photo ionization (ionization caused by light energy). Photons of short wavelength (that is, of high frequency) are absorbed by atmospheric gases. A portion of the energy is used to eject an electron, converting a neutral atom or molecule to a pair of charged species an electron, which is negatively charged, and a companion positive ion (Rees, 1989). The solar radiation that travels through the Earth's atmosphere is absorbed and the net concentration of free electrons is determined by the ionization output and loss mechanism. That is, photoionization, photo dissociation and their combination (dissociative photoionization) are the most important absorption processes (Prolss, 2006).

- Photoionization ($\lambda \leq$103 nm)
- Photo dissociation ($\lambda \leq$242 nm)
- Dissociative photoionization ($\lambda \leq$72 nm)

The intensity of the solar radiation at a wave length λ be $I(\lambda, z)$ in units of photons $m^2 s^{-1}$ at an altitude z .

$$n = n_o exp(\frac{-(z - z_o)}{H})$$

where $z_o = 0$ where n_o and T_o are the number and density and temperature at the reference height z_o respectively

$$n = n_o exp(\frac{z}{H}) \tag{3.5.1}$$

Where H is the scale height, and n_o the density at some reference height $z_o = 0$. The intensity is measured in eV/m^2s. There will be a cross-section $\sigma(\lambda)$ (m^2) for ionizing of neutral particles in the atmosphere by radiation at wavelength λ. Solar radiation at wavelength λ will therefore ionize a number of neutral particles per cubic meter and second (Brekke, 2012).

$$\frac{dI}{ds} = -n\sigma I \tag{3.5.2}$$

Where the minus sign indicates that the decreasing intensity from the Sun and the absorption cross-section σ depends on the wave length for a given molecule or atom. If the ionization enters the atmosphere at a zenith angle (χ)

$$ds = -\frac{dz}{cos(x)} = -sec(x)dz, \tag{3.5.3}$$

Let us assume that for every unit energy absorbed of radiation, there will be formed a number C electrons. Then the production of electrons per cubic meter and second can be expressed as:

$$q = c.\sigma.n.I = c\frac{dI}{ds} \tag{3.5.4}$$

C is called the ionization efficiency We now realize that since n increases and I decreases as we go down in the atmosphere, the product nI must reach a maximum

The equation 3.5.3 becomes,

$$\frac{dI}{I} = \sigma n ds = \sigma n sec(x) dz \tag{3.5.5}$$

Using the notation I_∞ for the intensity at the top of the atmosphere ($z = \infty$) we have,

$$\int_{I_\infty}^{I} \frac{dI}{I} = \sigma sec(x) \int_{\infty}^{Z} n(Z) dz \tag{3.5.6}$$

The integration gives

$$\ln \frac{I}{I_\infty} = -\sigma n H secx \tag{3.5.7}$$

from the height of maximum ionization

$$\ln \frac{I_m}{I_\infty} = -\sigma . n_m . H secx = -1 \tag{3.5.8}$$

$$I(z) = I_\infty exp[\sigma sec(x) \int_{z}^{\infty} n(Z) dz] \tag{3.5.9}$$

For the case of atmosphere compared of a single neutral species and in an isothermal ,the number density at the reference altitude z_o is given by:

$$n = n_o exp[\frac{-z - z_o}{H}] \tag{3.5.10}$$

Then substitute equation 3.5.10 in to equation 3.5.9 we get

$$I(z) = I_\infty exp[\sigma sec(x) n_o \int_{z}^{\infty} exp(\frac{-z - z_o}{H}) dz] \tag{3.5.11}$$

$$I(z) = I_\infty exp[-\sigma H sec(x) n_o exp(\frac{-z - z_o}{H}) dz] = I_\infty exp[-\sigma H sec(x) n(z) \tag{3.5.12}$$

$$I(z) = I_\infty exp[\tau] \tag{3.5.13}$$

where τ is the optical depth that measures of the proportion of radiation observed along the path through a partial transparent medium and is given by

$$\tau(z) = \sigma H n(z) sex(x) \tag{3.5.14}$$

3.6 Chapman ion production

Sydney Chapman presented in 1931 a simple mathematical model for the formation of ionized layers, which was based on the fact that energetic photons from the Sun split air molecules into electrons and positive ions (Zolesi, 2014). The model describes the major characteristics of the observed variations in the different layers of the ionosphere. He proposed the classical theory of ionospheric ionization by photoionization. This theory presupposes that the atmosphere is isothermal and obeys the hydrostatic equation so that the scale height H is independent of altitude in order to derive the classical Chapman formula for the ion production rate q. As previously stated the total number of photons absorbed per second $InAds$ is the unit time in a slab with area A and thickness ds. As a result, the total σnI represents the number of photons absorbed per unit volume per unit time (Brekke, 2012).

The ion production rate at maximum can be expressed as,

$$q_m == c.\sigma n_m I_m = c\sigma n_m \frac{I_\infty}{e} = \frac{c}{e}\frac{I_\infty}{e}\frac{I_\infty}{H} cosx \tag{3.6.1}$$

$$q_{mo} = \frac{c}{e}\frac{I_\infty}{H}$$

$$q_m = q_{m,o} cosx \tag{3.6.2}$$

Production at maximum can never be larger than for an overhead Sun and it decreases as cos θ for increasing zenith angle θ. based on equation 3.5.1 the ratio becomes,

$$\frac{n}{n_m} = e^{(-\frac{z-zm}{H})} \tag{3.6.3}$$

Then the production q at height z can then be expressed as

$$q = q_m exp(-\frac{z - z_m}{H}) exp[1 - exp(-\frac{z - z_m}{H})]$$

$$q = q_m exp[1 - \frac{z - z_m}{H} - exp(-\frac{z - z_m}{H})] \tag{3.6.4}$$

Substituting the normalized height reduced to the height of maximum ionization when $y = \frac{Z - Z_m}{H}$

$$q = q_m exp[1 - y - exp(-y)]$$

inserting $(\frac{z_m}{H})$ from equation 3.5.7 into 3.6.4

$$q = q_m exp[1 - \frac{z - z_{m,o}}{H} + \ln secx - exp(-\frac{z - z_{m,o}}{H} + \ln secx)]$$

$$q = q_m \; secx \; exp[1 - \frac{z - z_{m,o}}{H} - secx \; exp(-\frac{z - z_{m,o}}{H})] \tag{3.6.5}$$

As a result, equation 3.6.5 is the Chapman function, which demonstrates that the highest production occurs at $x = 0$ (when the Sun is directly overhead) and at the peak of highest ion production. That means the Chapman ionization profile for different solar zenith angles demonstrates that in an isothermal atmosphere, the height of the peak production rate increases as the solar zenith angle increases, but the rate of ionization drops, as shown in the Fig 3.3.

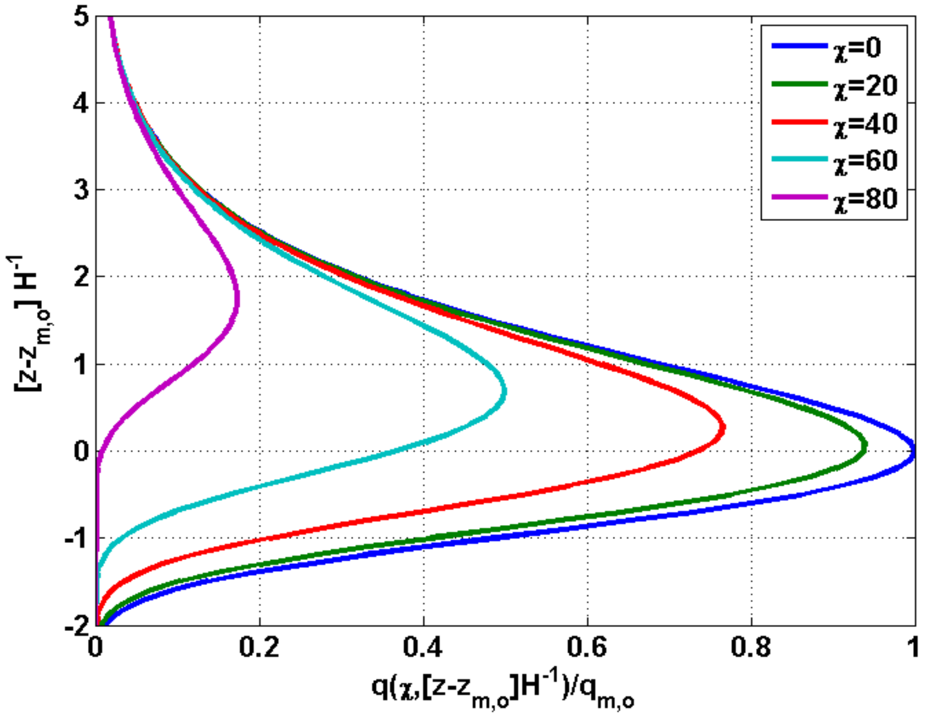

Figure 3.3: The chapman ionization profile for different solar zenith angle

3.7 Ionospheric Measuring Instruments

Nowadays, there are plenty of ionospheric probing instruments. Among these, Global Positioning System, Ionosond and In-situ measurement are some of them which are widely used. In this thesis, we have used data of ionospheric vTEC extracted from GPS. Thus, the following subsection briefs about the basics of GPS.

The Global Positioning System (GPS)

The GPS is a space-based radio navigation system that provides appropriately equipped users with three-dimensional position, navigational capabilities, and time information in all weather conditions (Bhatta, 2010). GPS is a positioning system based on a network of satellites that continuously transmit coded information. This information transmitted from the satellites can be interpreted by receivers to precisely identify locations on earth by measuring distances from the satellites (?). In order to obtain its coordinates, the receivers needs at least 4 satellites (see Fig 3.4) to solve for the 3 coordinates plus its own clock bias with respect to the GPS time scale. The GPS satellites are deployed and operated by the US Department of Defense (DoD) to satisfy the requirement for the military forces to accurately determine their position, velocity and time in common reference system Hofmann et al. (2012) and it is now used widely in both the military and civilian purposes.

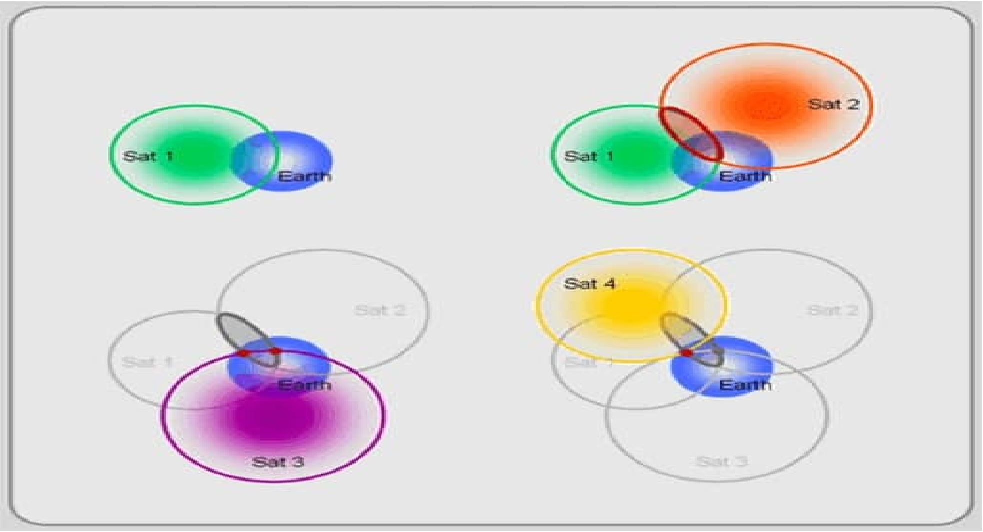

Figure 3.4: Global positioning system

The Global Positioning System (GPS) can be described in terms of three principal (segments). See one by one.

The space segment is consists essentially of 24 satellites carrying atomic clocks (Ashby, 2003) and the number of satellites in the constellation of satellites orbiting at about a height of 20,000 km above the earths surface. Each GPS satellites transmits a signal, which has a number of components two sine waves(also known as carrier frequency), two digital codes, and navigation message (El, 2002). The main purpose of these coded signals is to allow for calculating travel time from the satellite to the

GPS receiver and due to the rotation of the Earth, a satellite will be at its initial starting position after 24 hours.

The Control Segment is comprised of a number of ground-based monitoring stations, which continually gather information from the satellites and its transmitted codes and wave forms (Ashby, 2003). This segment is responsible for operating the GPS with the primary function to update navigational message of the satellites and accumulating such information as the exact altitude, position, velocity and overall health of the orbiting satellites 24 hours a day (Klobuchar, 1996).

The user segment is made up of GPS receivers and the user community that used in a variety of civilian and a military application. GPS receiver converts the satellites signal in to position, velocity and time. This information is used for navigation, positioning, time dissemination and research (Cai, 2009). Each GPS receiver is equipped with an antenna, clock, hardware and software.

At any given time, at least four satellites are visible at or near the Earth, according to the system's architecture and structure. This is due to GPS observations of at least ft. A GPS satellite emits positioning signals on two L-band frequencies, L_1 (at 1575.42 MHz) and L_2, which require our equations to compute the receiver's position and time component (at 1227.60 MHz). The two carrier frequencies f_1 and f_2 are coherently derived from the same (atomic) clock driven oscillator with a fundamental frequency of, f_o =10.23 MHz. That is, f_1=154f_o =1575.42 MHz and f_2 =120f_o =1227.60 MHz (Van Melle, 1995). Each GPS satellite transmits two Pseudo Random Noise (PRN) codes (Precise, P and Coarse Acquisition, C/A codes) and a navigation message for its identification and position determination respectively. Single frequency receivers track the C/A code only on the L1/f1 frequency and mathematical algorithms incorporated into the receivers hardware are needed to estimate ionospheric delay. Alternatively, the ionospheric delay for single frequency receivers can be estimated by applying an external correction to the position solution (Meggs et al., 2005). On the other hand, military dual frequency receivers track both PRN codes and the ionospheric delay can be estimated directly by comparing the delays on the L_1 and L_2 frequencies (Komjathy, 1997). GPS is one way of ranging system, the fundamental observable is the signal travel time between the satellite and the receiver and the travel time is converted to a range measurement using the signal propagation velocity. Therefore, for the estimation of TEC, dual frequency receivers are preferred, since they are designed to eliminate ionospheric error which is also the major source of error in GPS measurements.

The GPS measurements can be derived using two fundamental observations; pseudo range(P) and carrier phase(Φ). The different GPS error sources are the Satellite-dependent errors include orbital errors and satellite clock errors, medium-dependent errors include ionospheric and tropospheric delays, and receiver-dependent errors include reception noise, receiver clock error, multi path error, and antenna phase center changes.

Chapter 4

Data and Methods

4.1 Data Source

This thesis is aimed at modeling and predicting of vTEC with respect to F10.7 and Dst. We have used ground based Global Positioning System(GPS) vTEC data from Bahir Dar station (geographic $11.6^o N, 37.38^o E$) in the year 2010-2014. The raw data were obtained from `http://www.unavco.org`. The modeling part of vTEC was done by considering the corresponding F10.7 and Dst data which is available in `https://omniweb.gsfc.nasa.gov/form/dx1.html`.

4.2 Methods of Modeling

4.2.1 Multivariate Quadratic Polynomial Fitting

In polynomial regression modeling, multiple linear regression is also used. A polynomial, additive relationship between the dependent and a set of k independent variables $(x_j, j = 1 \text{ to } k)$ can explain this behavior of a dependent variable y. The general form of a complete second degree polynomial regression model in two variable x_1, x_2 may be expressed as

$$\mu_(y|(x_1, x_2)) = b_o + b_1 x_1 + b_2 x_2 + b_3 x_1^2 + b_4 x_2^2 + b_5 x_1 x_2$$

where $\mu_(y|(x_1, x_2))$=true mean response
b_j=model parameters j=0,1,2,3,4,5
x_j=independent variables j=1,2

The second degree polynomial includes the linear terms are x_1, x_2, second degree terms x_1^2, x_2^2, and the interaction term x_1x_2. The estimated model written as

$$\hat{y} = b_o + b_1x_1 + b_2x_2 + b_3x_1^2 + b_4x_2^2 + b_5x_1x_2$$

where $\hat{y}$=estimator of the mean response$\mu_(y|(x_1, x_2))$
b_j= estimators of the model parameters β_j for j=0,1,2,3,4,5
x_j= independent variables j=1,2

Before the model parameter estimators are found by minimizing the sum of squares of errors(SSE)

$$SSE = \sum_{i=1}^{n} e_i^2 = \sum_{i=1}^{n}(y_i - b_o - b_1x_{1i} - b_2x_{2i} - b_3x_{1i}^2 - b_4x_{2i}^2 - b_5x_{1i}x_{2i})^2$$

Where y_i= individual response of the i^{th} sample
x_{1i}, x_{2i}=i^{th} sample value of the independent variable n=sample size, number of observations then we set the partial derivatives equal to zero

$$\frac{\partial SSE}{\partial b_o} = 0,$$

$$\frac{\partial SSE}{\partial b_1} = 0,$$

$$\vdots$$

$$\frac{\partial SSE}{\partial b_5} = 0,$$

The system of linear equations in $(k+1=6)$ unknown $(b_o,....b_5)$

$$b_o + b_1\sum_{i=1}^{n} x_{1i} + b_2\sum_{i=1}^{n} x_{2i} + b_3\sum_{i=1}^{n} x_{1i}^2 + b_4\sum_{i=1}^{n} x_{2i}^2 + b_5\sum_{i=1}^{n} x_{1i}x_{2i} = \sum_{i=1}^{n} y_i$$

$$b_o\sum_{i=1}^{n} x_{1i} + b_1\sum_{i=1}^{n} x_{1i}^2 + b_2\sum_{i=1}^{n} x_{1i}x_{2i} + b_3\sum_{i=1}^{n} x_{1i}^3 + b_4\sum_{i=1}^{n} x_{1i}x_{2i}^2 + b_5\sum_{i=1}^{n} x_{1i}^2x_{2i} = \sum_{i=1}^{n} x_{1i}y_i$$

$$b_o\sum_{i=1}^{n} x_{2i} + b_1\sum_{i=1}^{n} x_{1i}x_{2i} + b_2\sum_{i=1}^{n} x_{2i}^2 + b_3\sum_{i=1}^{n} x_{1i}^2x_{2i} + b_4\sum_{i=1}^{n} x_{2i}^3 + b_5\sum_{i=1}^{n} x_{1i}x_{2i}^2 = \sum_{i=1}^{n} x_{2i}y_i$$

$$b_o\sum_{i=1}^{n} x_{1i}^2 + b_1\sum_{i=1}^{n} x_{1i}^3 + b_2\sum_{i=1}^{n} x_{1i}^2x_{2i} + b_3\sum_{i=1}^{n} x_{1i}^4 + b_4\sum_{i=1}^{n} x_{1i}^2x_{2i}^2 + b_5\sum_{i=1}^{n} x_{1i}^3x_{2i} = \sum_{i=1}^{n} x_{1i}^2y_i$$

$$b_o\sum_{i=1}^{n} x_{2i}^2 + b_1\sum_{i=1}^{n} x_{1i}x_{2i}^2 + b_2\sum_{i=1}^{n} x_{2i}^3 + b_3\sum_{i=1}^{n} x_{1i}^2x_{2i}^2 + b_4\sum_{i=1}^{n} x_{2i}^4 + b_5\sum_{i=1}^{n} x_{1i}x_{2i}^3 = \sum_{i=1}^{n} x_{2i}^2y_i$$

$$b_o\sum_{i=1}^{n} x_{1i}x_{2i} + b_1\sum_{i=1}^{n} x_{1i}^2x_{2i} + b_2\sum_{i=1}^{n} x_{1i}x_{2i}^2 + b_3\sum_{i=1}^{n} x_{1i}^3x_{2i} + b_4\sum_{i=1}^{n} x_{1i}x_{2i}^3 + b_5\sum_{i=1}^{n} x_{1i}^2x_{2i}^2 = \sum_{i=1}^{n} x_{1i}x_{2i}y_i$$

With regard to the elements that can be calculated from the results, the left side of the equation system forms a symmetrical square matrix. We can also see that a two variable multiple linear regression model is implemented in the linear equation system. The square matrix consists of the first three columns and rows and the first three elements on the right hand side.

The system can be represented using matrix notation with three matrices A,b and c as follows;

$$A = \begin{bmatrix} n & \sum_{i=1}^n x_{1i} & \sum_{i=1}^n x_{2i} & \sum_{i=1}^n x_{1i}^2 & \sum_{i=1}^n x_{2i}^2 & \sum_{i=1}^n x_{1i}x_{2i} \\ \sum_{i=1}^n x_{1i} & \sum_{i=1}^n x_{1i}^2 & \sum_{i=1}^n x_{1i}x_{2i} & \sum_{i=1}^n x_{1i}^3 & \sum_{i=1}^n x_{1i}x_{2i}^2 & \sum_{i=1}^n x_{1i}^2x_{2i} \\ \sum_{i=1}^n x_{2i} & \sum_{i=1}^n x_{1i}x_{2i} & \sum_{i=1}^n x_{2i}^2 & \sum_{i=1}^n x_{1i}^2x_{2i} & \sum_{i=1}^n x_{2i}^3 & \sum_{i=1}^n x_1ix_2i^2 \\ \sum_{i=1}^n x_{1i}^2 & \sum_{i=1}^n x_{1i}^3 & \sum_{i=1}^n x_{1i}^2x_{2i} & \sum_{i=1}^n x_{1i}^4 & \sum_{i=1}^n x_{1i}^2x_{2i}^2 & \sum_{i=1}^n x_{1i}^3x_{2i} \\ \sum_{i=1}^n x_{2i}^2 & \sum_{i=1}^n x_1ix_{2i}^2 & \sum_{i=1}^n x_{2i}^3 & \sum_{i=1}^n x_{1i}^2x_{2i}^2 & \sum_{i=1}^n x_{2i}^4 & \sum_{i=1}^n x_{1i}x_{2i}^3 \\ \sum_{i=1}^n x_{1i}x_{2i} & \sum_{i=1}^n x_{1i}^2x_{2i} & \sum_{i=1}^n x_{1i}x_{2i}^2 & \sum_{i=1}^n x_{1i}^3x_{2i} & \sum_{i=1}^n x_{1i}x_{2i}^3 & \sum_{i=1}^n x_{1i}^2x_{2i}^2 \end{bmatrix}$$

the matrix (variables) of b

$$b = \begin{bmatrix} b_0 \\ b_1 \\ b_2 \\ b_3 \\ b_4 \\ b_5 \end{bmatrix}$$

The right hand side (RHS) matrix (vector) c

$$c = \begin{bmatrix} c_0 \\ c_1 \\ c_2 \\ c_3 \\ c_4 \\ c_5 \end{bmatrix}$$

$$= \begin{bmatrix} \sum_{i=1}^{n} y_i \\ \sum_{i=1}^{n} x_1 i y_i \\ \sum_{i=1}^{n} x_2 i y_i \\ \sum_{i=1}^{n} x_1 i^2 y_i \\ \sum_{i=1}^{n} x_2 i^2 y_i \\ \sum_{i=1}^{n} x_1 i x_2 i y_i \end{bmatrix}$$

All elements of the A and c matrices in the above matrices are detrimental to the data. The linear equation method in matrix form is solved by the following matrix operation for vector b:

$$Ab = c \Longrightarrow A^{-1}Ab = A^{-1}c \Longrightarrow Ib = A^{-1}c \Longrightarrow b = A^{-1}c$$

where A=coefficient matrix, size $(k+1) \times (k+1)$
b=vector of unknowns, size $(k+1) \times 1$
c=right-hand-side or resource vector, size $(k+1) \times 1$
A^{-1}=an inverse of matrix A' such that $A^{-1}A = I$
I=identity or unit matrix, size $(k+1) \times (k+1)$

4.2.2 TEC Extraction From GPS

The Faraday rotation effect on a linear Polarized propagating plane wave has been used to estimate TEC for decades. However, due to the GPS observation network's excellent global coverage, TEC measurements are now largely conducted using GPS data (Rama Rao et al., 2006). Currently, there are about 32 GPS satellites orbiting the Earth at a time 55^o inclination and at an altitude of 20,200 km, they relay information on two signals of the frequency carrier, which are 1575.42 MHz (referred to as f_1) and 1227.60 MHz (referred to as f_2) respectively. Correspondingly two distances provided by GPS observations are (known as pseudo range) and measurements of two phases which correspond to the two signals.

The number of free electrons along the path of a signal from the satellite to receiver influences a radio signal's propagation speed. the number of free electrons with in a tube, with cross section $1m^2$ extending from the satellite to the receiver can be defined as the Total electron content (TEC) or Slant Total electron content (sTEC).

$$sTEC = \int_s^R Nedp,$$

Where Ne is the variable electron density along the path of the signal, and integration is along the signal path from the satellite to receiver, dp.

Now substitute sTEC into the phase delay and group delay phase delay(D_{ph}) and group delay(D_{gr})

$$D_{ph} = -\frac{40.3}{f^2} \int N_e dp$$

$$D_{gr} = \frac{40.3}{f^2} \int N_e dp$$

then the equation becomes;

$$D_{ph} = -\frac{40.3}{f^2} sTEC$$

$$D_{gr} = \frac{40.3}{f^2} sTEC$$

The receivers at GPS stations record signals transmitted at two L-band frequencies namely, f_1 and f_2 The time delay occurring during the propagation of these signals through the ionosphere is converted to pseudo-ranges and reported as P_1 and P_2 signals.

As different studies Ciraolo et al. (2007); Mannucci et al. (1998) show that the GPS measurements are used to estimate the TEC along a ray path between a GPS satellite and receiver on the ground. These GPS measurements can be recorded using either single or dual frequency GPS receivers. However, to eliminate ionospheric errors in the estimation of TEC dual frequency receivers are better (Klobuchar, 1996)over, by computing the differential phases of the code and carrier phase measurements, dual frequency GPS receivers can provide integral information about the ionosphere and plasma sphere (Ciraolo et al., 2007; Nahavandchi, 2008). Hence, in this paper, the GPS-TEC data have been obtained from dual frequency receiver using pseudo-range and carrier phase measurements.

$$P_{1,u}^{m} = \rho_u^m + c(\delta t_u - \delta t^m) + d_{trop,u}^{m} + d_{ion,u}^{m} + c(\varepsilon_1^m + \varepsilon_{1,u}) \tag{4.2.1}$$

$$P_{2,u}^{m} = \rho_u^m + c(\delta t_u - \delta t^m) + d_{trop,u}^{m} + d_{ion,u}^{m} + c(\varepsilon_2^m + \varepsilon_{2,u}) \tag{4.2.2}$$

where u denotes the receiver station index m denotes the satellite index. ρ is the actual range between satellite and receiver, δt_u and δt^m are the clock errors for the receiver and satellite, respectively. d_trop and d_ion are the troposphere and ionosphere group delays, respectively. ε^m and ε_u are the frequency-dependent satellite and receiver biases.

The model for GPS recordings also include antenna pattern and noise errors. The difference of Eqs 4.2.1 and 4.2.2 is called the geometry free linear combination of pseudo-range because the actual range rho is eliminated as

$$P_{4,u}^{m} = P_{2,u}^{m} - P_{1,u}^{m} = d_{ion2,u}^{m} - d_{ion1,u}^{m} + c(\varepsilon_2^m - \varepsilon_1^m) + c(\varepsilon_{2,u} - \varepsilon_{1,u}) \tag{4.2.3}$$

The tropospheric contribution $d_{trop,u}^{m}$ in Eqs 4.2.1 and 4.2.2 and any other source of error are also eliminated since they are not a function of frequency. Using satellite and receiver biases for f_1 and f_2 frequency signals, inter frequency or differential code biases (DCBs) are defined for the satellite and receiver as follows:

$$DCB^m = \varepsilon_1^m - \varepsilon_2^m \tag{4.2.4}$$

$$DCB_u = \varepsilon_{2,u} - \varepsilon_{1,u} \tag{4.2.5}$$

$$L^m_{1,u} = \lambda_1 \phi^m_{1,u} = P^m_u + c(\delta t_u - \delta t^m) + \lambda_1 \phi^m_{ion1,u} - c(\varepsilon^m_1 + \varepsilon_{1,u}) + \lambda_1 N^m_1 \tag{4.2.6}$$

$$L^m_{2,u} = \lambda_2 \phi^m_{2,u} = P^m_u + c(\delta t_u - \delta t^m) + \lambda_2 \phi^m_{ion2,u} - c(\varepsilon^m_2 + \varepsilon_{2,u}) + \lambda_2 N^m_2 \tag{4.2.7}$$

Where λ_1 and λ_2 are the wavelengths corresponding to f_1 and f_2 frequencies, $\phi^m_{1,u}$ and $\phi^m_{2,u}$ are the ionospheric phase delays corresponding to f_1 and f_2 frequencies, respectively. The N^m_1 and N^m_2 denote the initial phase ambiguity corresponding to f_1 and f_2 frequencies, respectively for the m^{th} satellite. Finally, $\phi^m_{trop,u}$ is the phase delay due to troposphere. The difference of Eqs 4.2.6 and 4.2.7 is called the geometry free linear combinations of phase delay and is given by

$$L^m_{4,u} = \lambda_1 \phi^m_{1,u} - \lambda_2 \phi^m_{2,u} = \lambda_1 \phi^m_{ion1,u} - \lambda_2 \phi^m_{ion2,u} + c(DCB^m) + c(DCB_u) + \Delta N^m \tag{4.2.8}$$

where ΔN^m is

$$\Delta N^m = \lambda_1 N^m_1 + \lambda_2 N^m_2 \tag{4.2.9}$$

Using the approximation given by

$$D^m_{ion,u} = -\phi^m_{1,u} \frac{c}{f} \approx A \frac{sTEC^m_u}{f^2} \tag{4.2.10}$$

$$P_{4,u} = A(\frac{f_1^2 - f_2^2}{f_1^2 f_2^2}) sTEC^m_u - c(DCB^m + DCB_u) \tag{4.2.11}$$

$$L^m_{4,u} = A(\frac{f_1^2 - f_2^2}{f_1^2 f_2^2}) sTEC^m_u - c(DCB^m + DCB_u) + \Delta N^m \tag{4.2.12}$$

For a chosen estimation time, incline Beam add up to Electron content (sTEC) can be calculated utilizing either pseudo-range or carrier stage information from each adherent. sTEC calculated from Eq 4.2.11 is loud and open to multi path impacts:

$$sTEC^m_u(n) = \frac{1}{A}(\frac{f_1^2 f_2^2}{f_1^2 - f_2^2})[P^m_{4,u}(n) + c(DCB^m + DCB_u)] \tag{4.2.13}$$

where the index n denotes the time sample, and 1 ≤ n ≤ N.

In Order to unravel sTEC from equation(4.2.12), the beginning equivocalness ΔN^m has to be settled. Within the works of the taking after standard strategy is utilized to begin with, a pattern, B, for each associated circular segment is gotten by differentiating pseudo-range and stage estimations as

$$B = \frac{1}{N_{me}} \sum_{n_{me}=1}^{N_{me}} (P_{4,u}^{m}(n_{me}) - L_{4,u}^{m}(n_{me})) \tag{4.2.14}$$

Where N_{me} is the number of estimations in a associated stage circular segment. At that point the incline TEC can be computed by inserting B into the phase equation (4.2.12) and sTEC can be extricated as

$$sTEC_u^m(n) = \frac{1}{A}(\frac{f_1^2 f_2^2}{f_1^2 - f_2^2})(B + L_{4,u}^m(n) + c(DCB^m + DCB_u)) \tag{4.2.15}$$

In the above conditions, u and m indicate the receiver and satellite. ids, individually, n is the estimation time. L_4 is the geometry free straight combination of carrier phase information and B is the standard esteem that's characterized in equation (4.2.15). DCB_u and DCB^m are the collector and adj. differential code inclinations individually. In Eq. (4.2.15), P_4 is the pseudo-range geometry free linear combination for double frequency GPS signals.

4.2.3 Correlation analysis between observed & estimated vTEC

We have applied multivariate quadratic model to estimate vTEC as a function of F10.7 and Dst. To show how good the estimated vTEC matched with the observed vTEC, we used different approaches. First we identified whether the quadratic model is appropriate or not by just plotting the observed vTEC data with respect to F10.7 and Dst (See Fig. 5.2). In most cases, the trends were both linear and non-linear and we concluded to apply quadratic polynomial model than linear one. Then after, we plotted stacked bar plots to see the pattern and magnitude correlation between modeled and observed vTEC for both short (daily values of vTEC for each year) and long-term (merged data of 2010-2014 years) data set. Besides, we have computed error bars and linear correlation coefficient to investigate the deviation between the observed and modeled vTEC. We also estimated hourly vTEC values by taking hourly GPS observations in the year 2011.

Chapter 5

Results and Discussions

5.1 Introduction

The ionosphere, ionized part of the upper atmosphere, could vary due to different solar and geomagnetic activities. According to different scholars such as Ngwira et al. (2012), Ma et al. (2007) and Judge et al. (1998) it may vary significantly due to the variations in solar activities, geomagnetic events, altitude as well as geographic orientations of ionospheric regions. One of the peculiar ionospheric parameter that can be used to demonstrate the above mentioned variations is its total electron content (TEC).

The purpose of this thesis is to model the variability of ionospheric TEC as a function of solar (F10.7) and geomagnetic (Dst) parameters over Bahir Dar, Ethiopia in the year 2010 to 2014. We used hourly and daily vTEC measurements from a GPS receiver deployed at Bahir Dar, Ethiopia. Multivariate quadratic model is employed to estimate the vTEC for both short- and long-term data set. The following sections will present the basic findings of the thesis with possible scientific discussions.

5.2 Daily variations (trends) of F10.7, Dst and vTEC

The temporal variations of Dst, F10.7 and vTEC are depicted by the top, middle and bottom panels of Fig. 5.1 respectively. All of the three parameters have showed clear day-to-day variations with minimum and maximum values for each year we considered. The variations of F10.7 can be associated with the strength of solar radiation which can be explained in terms of the orientation of solar zenith angle (McNamara , 1991; liu et al., 2007). The daily variations of Dst implies that there is geomagnetic activity that can be associated with the suppression of Earth's magnetic field due to particle or radiation storms originated from the sun.

Specifically, the vTEC have got its minimum during solstice and maximum during equinox days. The daily variations of vTEC can be attributed to the strength of solar radiation that can contribute significantly for ionization. Besides, geomagnetic activities could also brought such daily variations in the ionosphere. The seasonal observations might be associated again with the influence of neutral dynamics as well as the hemisphere based distribution of solar radiation. The Sun shines directly on the equator during Equinox, and the lengths of day and night are approximately identical, resulting in maximum photo-ionization and maximum TEC in the equatorial ionosphere and during solstice the Sun is not overhead at the equator, the light intensity passing through the ionosphere above the equator is lower than at the equinox, resulting in a lower TEC in the ionosphere, which causes several navigational and communication issues (Aragaw et al., 2019).

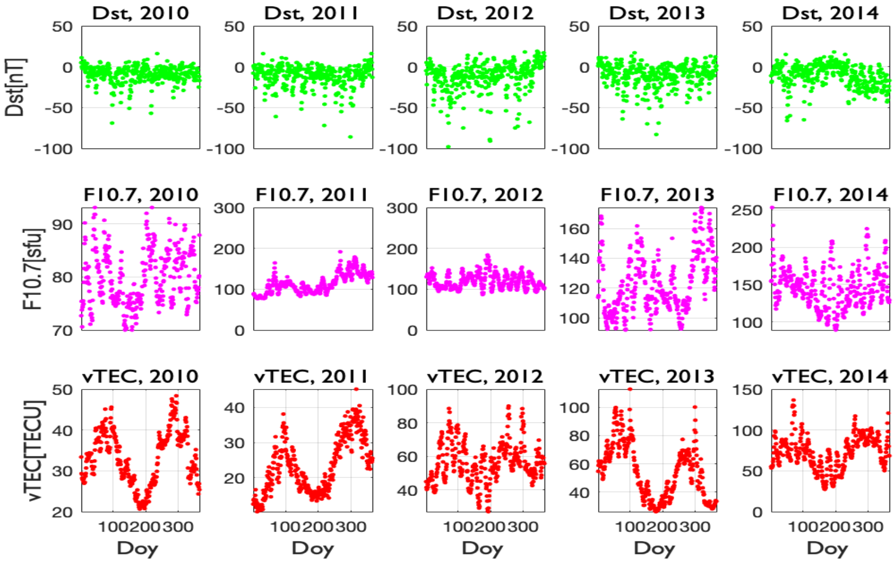

Figure 5.1: *Daily variations of geomagnetic (top), solar (middle) parameters and vTEC (bottom) for the year 2010 to 2014.*

Fig. 5.2 illustrates the linear and non-linear variations of daily vTEC as a function of F10.7 (top panel) and Dst (bottom panel) in the year 2010 to 2014. This scatter plot helped us to identify a model that best fit to the trend of the vTEC data. In our case, we applied quadratic model, specifically the multivariate one, to show the individual and simultaneous effect of solar (F10.7) and geomagnetic (Dst) activities. It clear that the coefficient of x^2 in quadratic model advocates the non-linear and that of x refers the linear trend. The simultaneous effect of F10.7 and Dst was inferred from the coefficients of x_1x_2.

Based on the top and bottom panels of this Fig. we intended to use multivariate quadratic model and estimated vTEC for each year. From these estimations, we could infer both the linear and non-linear variations of vTEC as a function of F10.7 and Dst. In most cases except in 2012, the trend in the variation of vTEC due to solar and geomagnetic parameters was both linear and non-linear, however, in 2012 it seems only linear in variation.

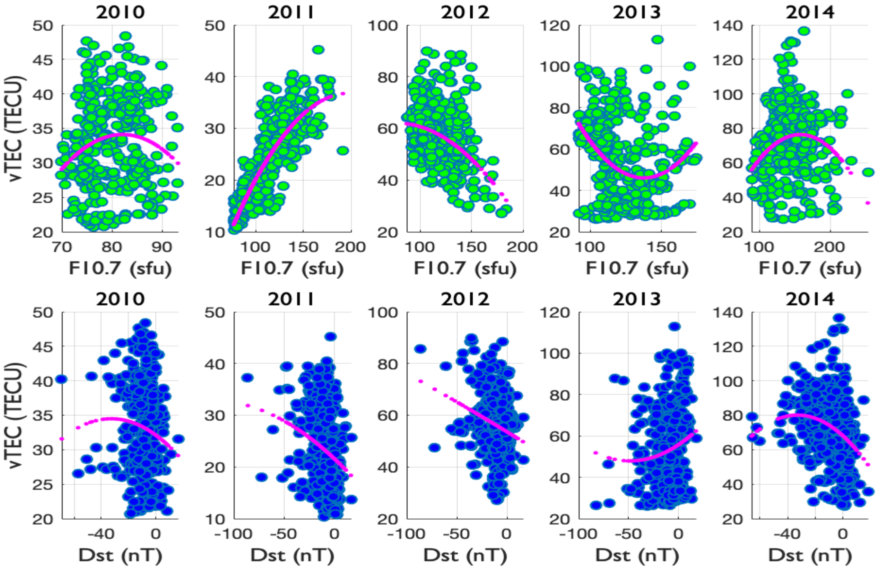

Figure 5.2: *Linear and non-linear trend of vTEC as a function of F10.7 (top) and Dst (bottom).*

5.3 Analysis on short-term Estimations

The short-term estimations was done for each year and displayed by Figs. 5.3, 5.4, 5.5, 5.6 and 5.7 for 2010, 2011, 2012, 2013 and 2014 respectively. The top panel of these Figs. illustrate the estimated vTEC using multivariate quadratic model (blue), the observed vTEC from GPS receiver (green) and the IRI-2016 ionospheric model vTEC (black) for the first 200 data points. The rest part of the data was used for validation purpose of the quadratic model output. The predicted/validated part of the modeled vTEC is given by magenta, the GPS data used for validation is displayed by the yellow color and the corresponding IRI-2016 vTEC data is showed by cyan color. From these Figs., one can clearly see how the modeled vTEC significantly explained the variations of the GPS observations. This can be seen in terms of length of the bars and pattern of the variations of vTEC in the model in accordance with the pattern of GPS vTEC.

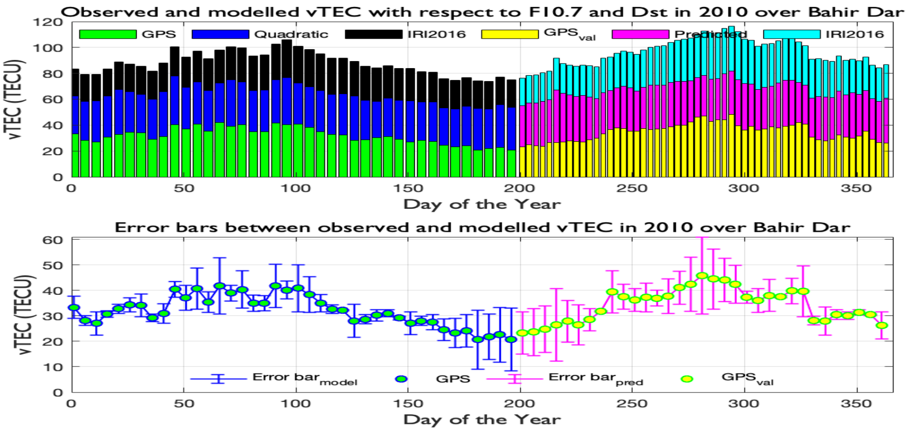

Figure 5.3: *Estimation of vTEC and error bar in 2010 over Bahir Dar, Ethiopia.*

The bottom panels of Figs. 5.3, 5.4, 5.5, 5.6 and 5.7 present the error bars computed that clearly show the deviation of the multivariate quadratic model from observed vTEC values. In some days minimum deviations were observed and in other days maximum deviations were recorded. Specifically maximum deviation between the estimated and observed vTEC values were observed during equinox days. This signifies the need for additional parameters, such as related with the dynamics of electric field, the influence of wind on the ionized plasma etc, in the modeling part so that deviations might be minimized significantly (Tariku, 2019).

Besides, the error was significant during solar maxima years. The quadratic model has given very good estimates during the year 2010 and 2011 compared to 2012, 2013 and 2014. This has also a message for ionospheric modeling world to consider some more parameters for solar maximum periods.

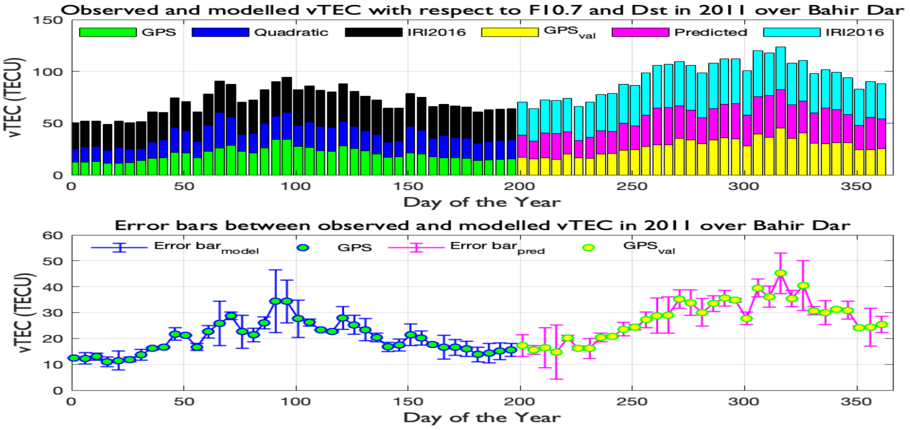

Figure 5.4: *Estimation of vTEC and error bar in 2011 over Bahir Dar, Ethiopia.*

We have also computed sample correlation coefficient between estimated and observed daily vTEC in the year 2011. It is depicted by Fig. 5.8. On average, the linear correlation coefficient was about 0.7. This implies that about 70% the variations of GPS vTEC could be explained by the multivariate quadratic model.

The non-linear and linear trends of the vTEC could be easily inferred from the magnitude of the coefficients of x^2 and x for both F10.7 and Dst inputs. These coefficients are illustrated in Fig. 5.9. The top left is for the year 2010, top right for 2011, bottom left for 2012 and bottom right for 2014 respectively. For these short-term daily estimations, the linear variation significantly dominate the none-linear one. The negative and positive coefficients of the linear term tell us the direct and indirect proportionality between the input parameters (Dst and F10.) and the modeled vTEC. As one can see from these Fig. such mixed proportionality was observed for both Dst and F10.7. The mixed proportionality of Dst with vTEC is expected because geomagnetic storms may have positive and negative effect on vTEC (Tsagouri, 2000). However, unexpected mixed proportionality between F10.7 and vTEC was observed as a unique result from our modeling. This implies that

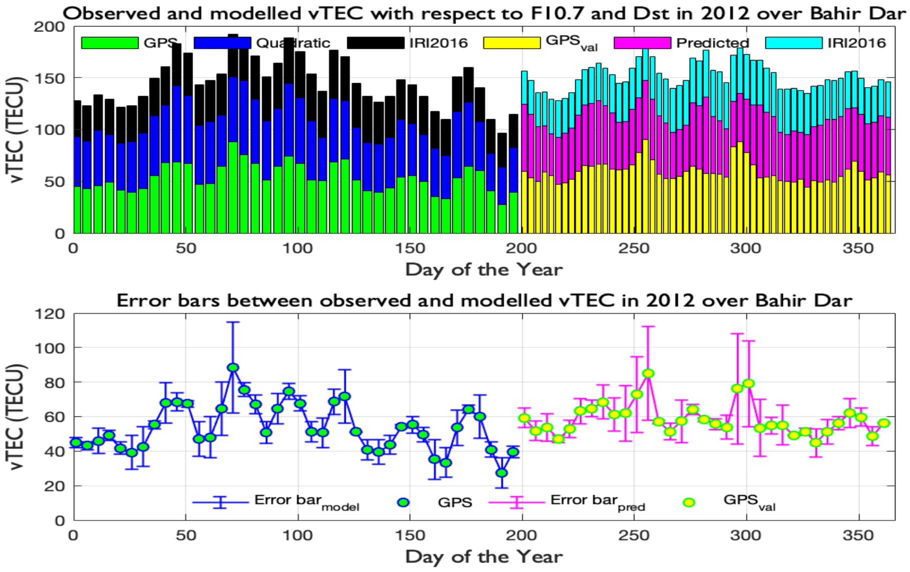

Figure 5.5: *Estimation of vTEC and error bar in 2012 over Bahir Dar, Ethiopia.*

there is still a need of extensive modeling investigations of vTEC as a function of solar activities. This result contradicts with (Kassa, 2017)

5.4 Analysis on long-term Estimations

We have also conducted a long-term estimation and analysis by merging the daily data of the five years (2010 to 2014). A total of 1825 data points were used to estimate the vTEC using multivariate quadratic model as a function of geomagnetic and solar parameters. The top panel of Fig. 5.10 illustrates the correlation between vTEC and F10.7, vTEC and Dst, distribution of Dst (top) the middle panel describes the temporal variation of F10.7 and the bottom panel shows the temporal variation of vTEC in 2010-2014 over Bahir Dar, Ethiopia. From the left-top and middle-top panel of this Fig., one can confirm the appropriateness of applying quadratic model for modeling the long-term vTEC variation. The middle and bottom panels of this

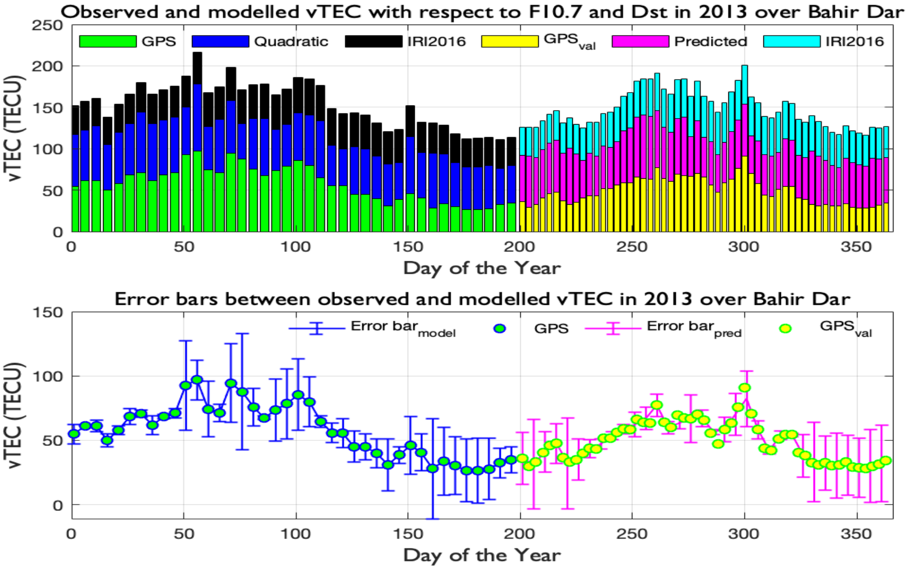

Figure 5.6: *Estimation of vTEC and error bar in 2013 over Bahir Dar, Ethiopia.*

Fig. tell us how F10.7 and vTEC have increasing as we go from solar minimum to maximum years. This means, there is an increasing trend of vTEC as a function of days. Here, the first day is 01 January 2010 and the last day is 31 December 2014. Particularly, the top-left and top-right panels clearly show the dominancy of non-linear variation over linear one during long-term data set estimation.

The quadratic model-based estimated (blue), GPS (green) and IRI2016 (black) vTECs are displayed by Fig. 5.11. From top panel of this Fig., we can infer how best the proposed quadratic model fits with the observed vTEC. Besides, the comparison the quadratic model with the IRI2016 is clearly seen.

The bottom panel of Fig. 5.11 illustrates to what extent the modeled vTEC deviates from the observed GPS vTEC values for each days of the years 2010 to 2014. In 2010, the deviation was minimum compared to that of other years. Specifically during the last days of the year 2014, the estimated vTEC has showed significant

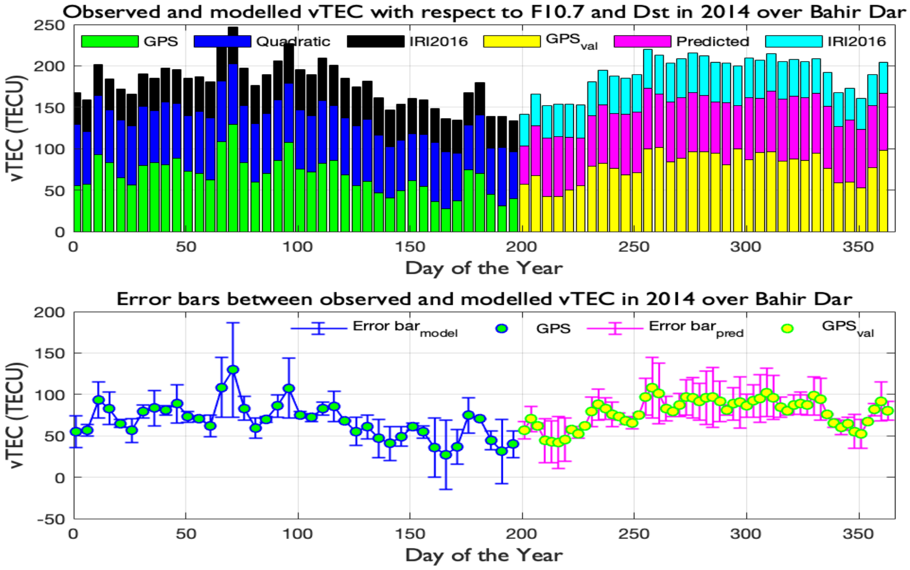

Figure 5.7: *Estimation of vTEC and error bar in 2014 over Bahir Dar, Ethiopia.*

deviation. This implies that, as we go up to the solar maximum years, the use of quadratic model lacks to describe the expected variations in vTEC. This result is inline with a report by (Olwendo , 2016).

5.5 Estimation on hourly data set in the year 2011

A similar estimation was done on hourly data set for the year 2011. A total of 8760 data points were used for this particular estimation. The estimated result is depicted by Fig. 5.12. A similar pattern with daily and merged data set estimation was observed. The top panel of this Fig. show how long the estimated (magenta) and observed (blue) are varied simultaneously within the given time of span.

The bottom panel of this Fig. illustrates the scatter plot of the estimated and observed vTEC in hourly basis data set in the year 2011. The linear correlation between the modeled and observed vTEC can be extracted from this plot. By looking

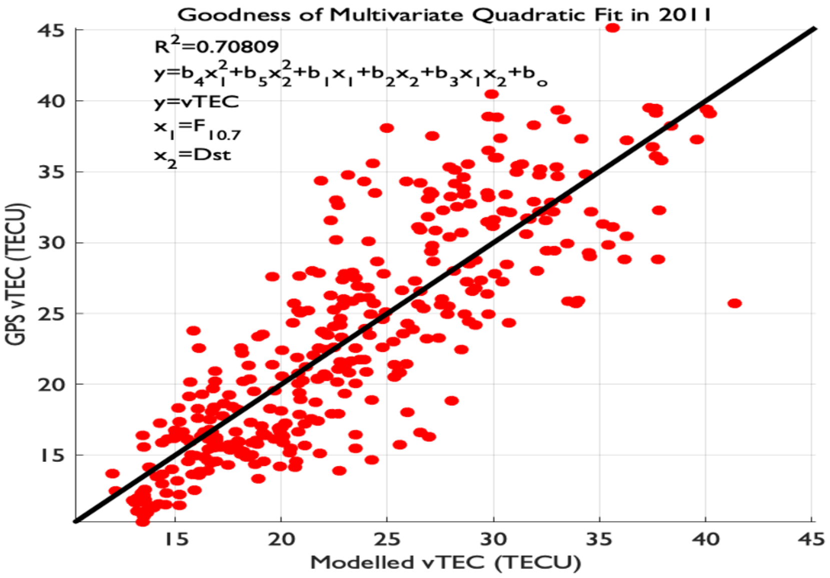

Figure 5.8: *Correlation coefficient between modeled (estimated) and observed vTEC in the year 2011 over Bahir Dar, ethiopia.*

at the slop of the fitted line (red color), one can see that the correlation coefficient is greater than 0.5 and is positive. This implies that at least 50% of the variation of the observed vTEC in hourly data set is explained by the quadratic model. However, in daily analysis, the mean correlation coefficient was about 0.7 implies that 70% of the variations was explained by the model using daily data set.

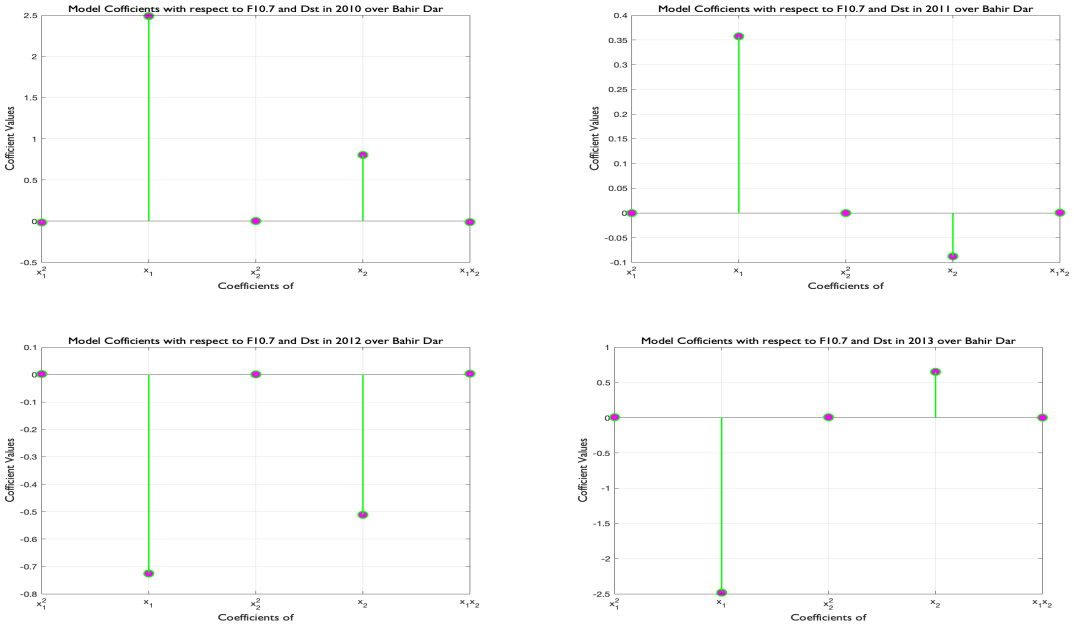
Model Cofficients with respect to F10.7 and Dst in 2010 over Bahir Dar

Model Cofficients with respect to F10.7 and Dst in 2011 over Bahir Dar

Model Cofficients with respect to F10.7 and Dst in 2012 over Bahir Dar

Model Cofficients with respect to F10.7 and Dst in 2013 over Bahir Dar

Figure 5.9: *Linear and non-linear coefficients of the quadratic model vTEC in the year 2010-2013 over Bahir Dar, ethiopia.*

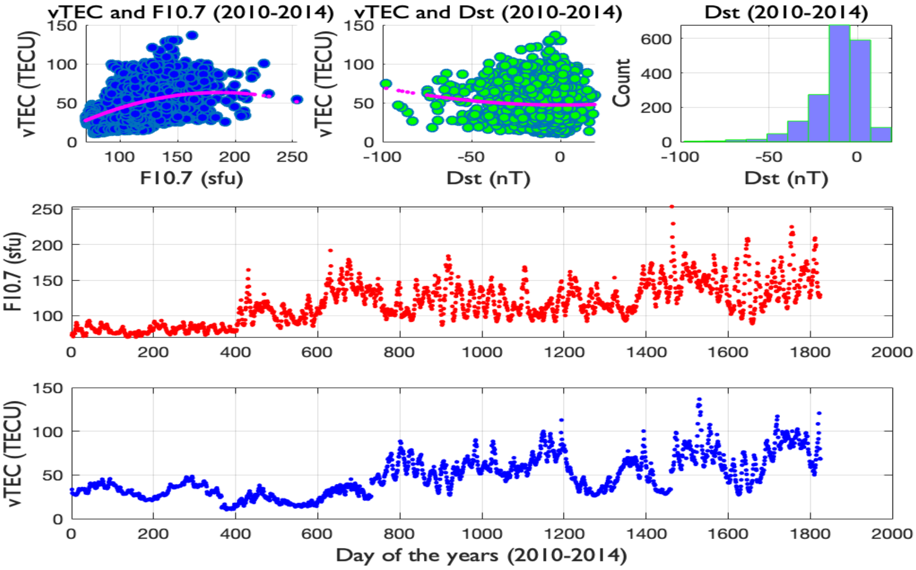

Figure 5.10: *(Top) Correlation between vTEC and F10.7, vTEC and Dst, distribution of Dst (top), (middle), temporal variation of F10.7 and (bottom), temporal variation of vTEC in 2010-2014 over Bahir Dar, Ethiopia.*

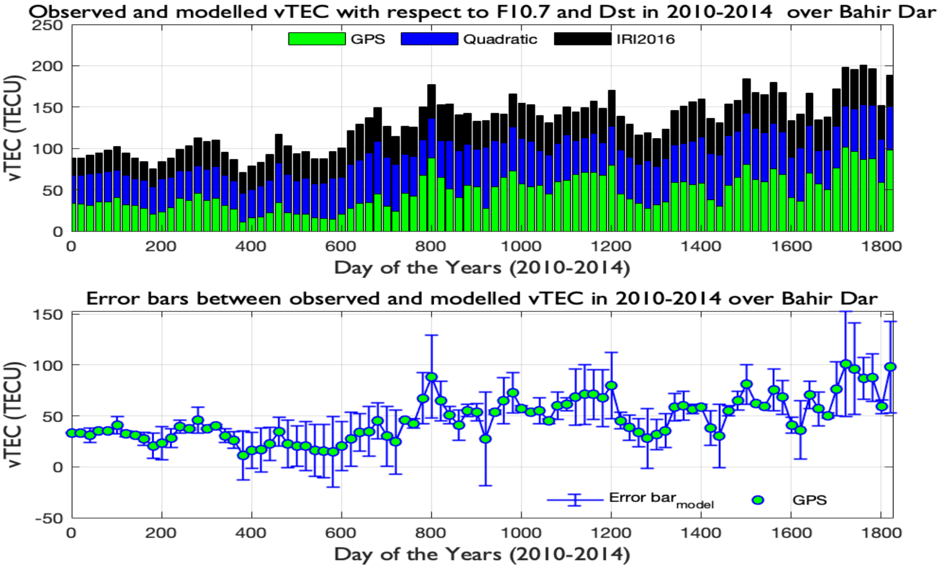

Figure 5.11: *Long-term estimation of vTEC over Bahir Dar, Ethiopia in 2010-2014.*

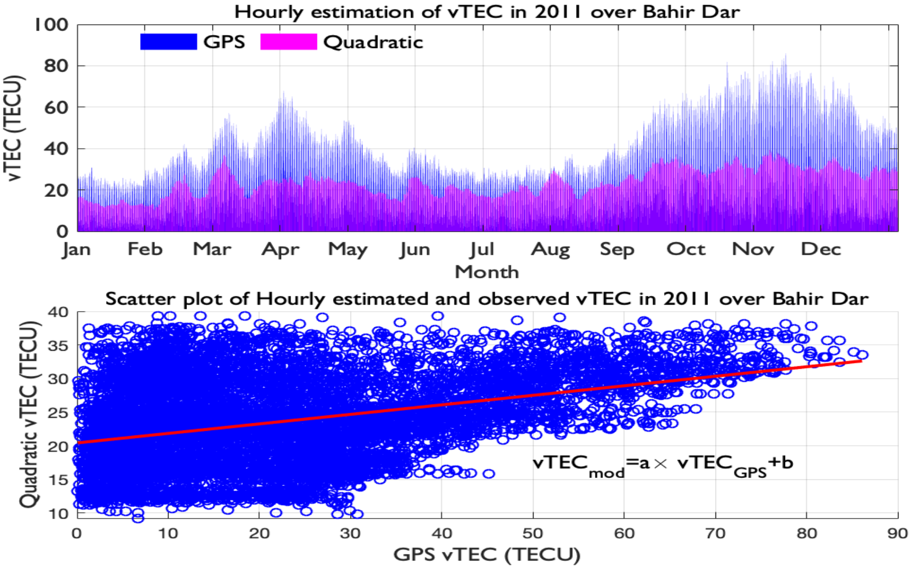

Figure 5.12: *Hourly estimation of vTEC over Bahir Dar, Ethiopia in 2011.*

Chapter 6

Conclusions and Recommendations

6.1 Conclusions

The ionosphere is a shell of electrons and electrically charged atoms and molecules produced as solar radiation interacts with the upper atmosphere of the Earth. The ionosphere is well known to vary significantly with altitude, latitude, longitude, universal time, season, solar cycle, and geomagnetic activity, and to exhibit considerable day-to-day variability. The Total electron content(TEC) is one of the parameters used to understand and investigate the spatial and temporal anomalies of ionospheric variability.

In the present study, we have estimated the daily and hourly vTEC values using multivariate quadratic model over Bahir Dar, Ethiopia in the year 2010 to 2014. The daily variations of vTEC as a function of F10.7 and Dst is modeled.

In our case, we applied quadratic model, specifically the multivariate one, to show the individual and simultaneous effect of solar (F10.7) and geomagnetic (Dst) activities. Through the modeling of vTEC, both the linear and non-linear trend of vTEC are captured.

The short term estimation was done for each year. This illustrate the estimated vTEC using multivariate quadratic model, the observed vTEC from GPS receiver and the IRI-2016 ionospheric model vTEC for the first 200 data points. The rest part of the data was used for validation purpose of the quadratic model output. We have displayed the error bars that demonstrate how the multivariate quadratic model deviates from observed vTEC values. Besides, the daily and seasonal variations in the deviation of the modeled vTEC was depicted. We come to conclude that the multivariate quadratic model is comparable with IRI-2016 vTEC outputs.

By combining the daily data of five consecutive years(2010 to 2014), we were able to undertake a long-term estimation and analysis. A similar estimation was done for hourly data set for the year 2011. As a result, almost similar influence was reached as of short and long term estimations. From this analysis, a linear correlation between the modeled and observed vTEC could be extracted.

6.2 Recommendations

The physics of ionospheric variability in the African sector has attracted the attentions of many research and still we do not understand it very well. Extensive observations and modeling of the variability are very important in shaping our approach. To fully understand the variability of vTEC in Ethiopian as well as East African sector, the task of modeling and the prediction should continue by considering more GPS station other than Bahir Dar. Besides, further input parameters related to the effect of wind dynamics and ionospheric electric field can be applied for improving our model.

Bibliography

Aars, J., & Ims, R. A. (2002). Intrinsic and climatic determinants of population demography: the winter dynamics of tundra voles. Ecology, 83(12), 3449-3456.

Afraimovich, E. L., Astafyeva, E. I., & Zhivetiev, I. V. (2006, July). Solar activity and global electron content. In Doklady earth sciences (Vol. 409, No. 2, p. 921). Springer Nature BV.

Akala, A. O., Somoye, E. O., Adewale, A. O., Ojutalayo, E. W., Karia, S. P., Idolor, R. O., ... & Doherty, P. H. (2015). Comparison of GPS-TEC observations over Addis Ababa with IRI-2012 model predictions during 20102013. Advances in Space Research, 56(8), 1686-1698.

Aragaw, M., Gebiregiorgis, A., & Tsegaye, K. (2019). Solar Activity and Geomagnetic Storm Effects on GPS Ionospheric TEC over Ethiopia. Momona Ethiopian Journal of Science, 11(2), 276-300.

AraujoPradere, E. A., FullerRowell, T. J., Codrescu, M. V., & Bilitza, D. (2005). Characteristics of the ionospheric variability as a function of season, latitude, local time, and geomagnetic activity. Radio Science, 40(5).

Ashby, N. (2003). Relativity in the global positioning system. Living Reviews in relativity, 6(1), 1-42.

Balan, N., Bailey, G. J., & Jayachandran, B. (1993). Ionospheric evidence for a nonlinear relationship between the solar euv and 10.7 cm fluxes during an intense solar cycle. Planetary and space science, 41(2), 141-145.

Bhatta, B. (2010). Global navigation satellite systems: insights into GPS, GLONASS, Galileo, Compass, and others. BS Publications.

Bilitza, D. (2000). The importance of EUV indices for the International Reference Ionosphere. Physics and Chemistry of the Earth, Part C: Solar, Terrestrial & Planetary Science, 25(5-6), 515-521.

Bilitza, D., McKinnell, L. A., Reinisch, B., & Fuller-Rowell, T. (2011). The international reference ionosphere today and in the future. Journal of Geodesy, 85(12), 909-920.

Brekke, A. (2012). Physics of the upper polar atmosphere. Springer Science & Business Media.

Cai, C. (2009, August). Precise point positioning using dual-frequency GPS and GLONASS measurements. In Masters Abstracts International (Vol. 48, No. 03).

CCIR, C. (1967). Atlas of ionospheric characteristics.

Chapman, S. (1931). The absorption and dissociative or ionizing effect of monochromatic radiation in an atmosphere on a rotating earth. Proceedings of the Physical Society (1926-1948), 43(1), 26.

Chen, Y., Liu, L., & Le, H. (2008). Solar activity variations of nighttime ionospheric peak electron density. Journal of Geophysical Research: Space Physics, 113(A11).

Ciraolo, L., Azpilicueta, F., Brunini, C., Meza, A., & Radicella, S. M. (2007). Calibration errors on experimental slant total electron content (TEC) determined with GPS. Journal of Geodesy, 81(2), 111-120.

Clette, F., Svalgaard, L., Vaquero, J. M., & Cliver, E. W. (2014). Revisiting the sunspot number. Space Science Reviews, 186(1), 35-103.

Coco, D. S., Gaussiran, T. L., & Coker, C. (1995). Passive detection of sporadic E using GPS phase measurements. Radio science, 30(6), 1869-1874.

Cummer, S. A. (2000). Modeling electromagnetic propagation in the Earth-ionosphere waveguide. IEEE Transactions on Antennas and Propagation, 48(9), 1420-1429.

Davies, K. (1990). Ionospheric radio (No. 31). IET.

Eby, L. T., Casper, W. J., Lockwood, A., Bordeaux, C., & Brinley, A. (2005). Work and family research in IO/OB: Content analysis and review of the literature (19802002). Journal of vocational behavior, 66(1), 124-197.

Eckler, P., & Bolls, P. (2011). Spreading the virus: Emotional tone of viral advertising and its effect on forwarding intentions and attitudes. Journal of Interactive Advertising, 11(2), 1-11.

El-Rabbany, A. (2002). Introduction to GPS: the global positioning system. Artech house.

Ermolli, I., Matthes, K., Dudok de Wit, T., Krivova, N. A., Tourpali, K., Weber, M., ... & Woods, T. N. (2013). Recent variability of the solar spectral irradiance and its impact on climate modelling. Atmospheric Chemistry and Physics, 13(8), 3945-3977.

Fleagle, R. G., & Businger, J. A. (1981). An introduction to atmospheric physics. Academic Press.

Fletcher, L., Dennis, B. R., Hudson, H. S., Krucker, S., Phillips, K., Veronig, A., ... & Temmer, M. (2011). An observational overview of solar flares. Space science reviews, 159(1-4), 19.

Forbes, J. M., Palo, S. E., & Zhang, X. (2000). Variability of the ionosphere. Journal of Atmospheric and Solar-Terrestrial Physics, 62(8), 685-693.

Foukal, P., North, G., & Wigley, T. (2004). A stellar view on solar variations and climate. Science, 306(5693), 68-69.

Gao, Y., & Liu, Z. Z. (2002). Precise ionosphere modeling using regional GPSNetwork data. Positioning, 1(03).

Gillaspy, J. D. (2001). Highly charged ions. Journal of Physics B: Atomic, Molecular and Optical Physics, 34(19), R93.

Goldman, B. D. (2001). Mammalian photoperiodic system: formal properties and neuroendocrine mechanisms of photoperiodic time measurement. Journal of biological rhythms, 16(4), 283-301.

Golub, L., & Pasachoff, J. M. (2010). The solar corona. Cambridge University Press.

Gombosi, T. I.,(1998). Physics of the space environment. Cambridge University Press.

Gorney, D. J. (1990). Solar cycle effects on the nearEarth space environment. Reviews of Geophysics, 28(3), 315-336.

Guo, J., Wan, W., Forbes, J. M., Sutton, E., Nerem, R. S., Woods, T. N., ... & Liu, L. (2007). Effects of solar variability on thermosphere density from CHAMP accelerometer data. Journal of Geophysical Research: Space Physics, 112(A10).

Habarulema, J. B. (2010). A contribution to TEC modelling over Southern Africa using GPS data (Doctoral dissertation, Rhodes University).

Haigh, J. D. (2007). The Sun and the Earths climate. Living reviews in solar physics, 4(1), 1-64.

Hale, G. E. (1908). No. 30. On the probable existence of a magnetic field in Sunspots. Contributions from the Mount Wilson Observatory/Carnegie Institution of Washington, 30, 1-29.

Hale, G. E., & Nicholson, S. B. (1925). The law of sun-spot polarity. The Astrophysical Journal, 62, 270.

Hathaway, D. H., Wilson, R. M., & Reichmann, E. J. (1994). The shape of the sunspot cycle. Solar Physics, 151(1), 177-190.

Hedin, A. E. (1984). Correlations between thermospheric density and temperature, solar EUV flux, and 10.7cm flux variations. Journal of Geophysical Research: Space Physics, 89(A11), 9828-9834.

Heldmaier, G., Steinlechner, S., Rafael, J., & Vsiansky, P. (1981). Photoperiodic control and effects of melatonin on nonshivering thermogenesis and brown adipose tissue. Science, 212(4497), 917-919.

Hochegger, G., Nava, B., Radicella, S., & Leitinger, R. (2000). A family of ionospheric models for different uses. Physics and Chemistry of the Earth, Part C: Solar, Terrestrial & Planetary Science, 25(4), 307-310.

Hofmann-Wellenhof, B., Lichtenegger, H., & Collins, J. (2012). Global positioning system: theory and practice. Springer Science & Business Media.

Hunsucker, R. D., & Hargreaves, J. K. (2007). The high-latitude ionosphere and its effects on radio propagation. Cambridge University Press.

Imada, S., Aoki, K., Hara, H., Watanabe, T., Harra, L. K., & Shimizu, T. (2013). Evidence for hot fast flow above a solar flare arcade. The Astrophysical Journal Letters, 776(1), L11.

Iribarne, J. V., & Cho, H. R. (2012). Atmospheric physics. Springer Science & Business Media.

Judge, D. L., McMullin, D. R., Ogawa, H. S., Hovestadt, D., Klecker, B., Hilchenbach, M., ... & Wurz, P. (1998). First solar EUV irradiances obtained from SOHO by the CELIAS/SEM. In Solar Electromagnetic Radiation Study for Solar Cycle 22 (pp. 161-173). Springer, Dordrecht.

Jursa, A. S. (1985). Handbook of geophysics and the space environment (Vol. 1). Hanscom Air Force Base, MA: Air Force Geophysics Laboratory, Air Force Systems Command, United States Air Force.

Kane, R. P. (1992). Sunspots, solar radio noise, solar EUV and ionospheric oF2. Journal of atmospheric and terrestrial physics, 54(3-4), 463-466.

Kassa, T., & Damtie, B. (2017). Ionospheric irregularities over Bahir Dar, Ethiopia during selected geomagnetic storms. Advances in Space Research, 60(1), 121-129.

Kelley, M. C. (2009). The Earth's ionosphere: plasma physics and electrodynamics. Academic press.

Kivelson, M. G., Kivelson, M. G., & Russell, C. T. (Eds.). (1995). Introduction to space physics. Cambridge university press.

Klobuchar, J. A. (1996). Ionospheric effects in Global Positioning System: theory and applications, Vol. I, ed. BW Parkinson and JJ Spilker, American Institute of Aeronautics and Astronautics, Washington, DC, USA.

Komjathy, A. (1997). Global ionospheric total electron content mapping using the Global Positioning System (Doctoral dissertation, University of New Brunswick).

Kumar, S., Priyadarshi, S., Krishna, S. G., & Singh, A. K. (2012). GPS-TEC variations during low solar activity period (20072009) at Indian low latitude stations. Astrophysics and Space Science, 339(1), 165-178.

Langley, R. B. (2000). GPS, the Ionosphere, and the Solar Maximum. GPS world, 11(7), 44-49.

Lean, J. L., Emmert, J. T., Picone, J. M., & Meier, R. R. (2011). Global and regional trends in ionospheric total electron content. Journal of Geophysical Research: Space Physics, 116(A2).

Lee, D. Y., Lyons, L. R., & Yumoto, K. (2004). Sawtooth oscillations directly driven by solar wind dynamic pressure enhancements. Journal of Geophysical Research: Space Physics, 109(A4).

Lei, J., Liu, L., Wan, W., & Zhang, S. R. (2005). Variations of electron density based on longterm incoherent scatter radar and ionosonde measurements over Millstone Hill. Radio science, 40(2).

Li, M., & Parrot, M. (2013). Statistical analysis of an ionospheric parameter as a base for earthquake prediction. Journal of Geophysical Research: Space Physics, 118(6), 3731-3739.

Lilensten, J., Dudok de Wit, T., Kretzschmar, M., Amblard, P. O., Moussaoui, S., Aboudarham, J., & Auchre, F. (2008, February). Review on the solar spectral variability in the EUV for space weather purposes. In Annales Geophysicae (Vol. 26, No. 2, pp. 269-279). Copernicus GmbH.

Liu, H., Stolle, C., Frster, M., & Watanabe, S. (2007). Solar activity dependence of the electron density in the equatorial anomaly regions observed by CHAMP. Journal of Geophysical Research: Space Physics, 112(A11).

Liu, Y. D., Luhmann, J. G., Kajdi, P., Kilpua, E. K., Lugaz, N., Nitta, N. V., ... & Galvin, A. B. (2014). Observations of an extreme storm in interplanetary space caused by successive coronal mass ejections. Nature Communications, 5(1), 1-8.

Ma, R. P., Ji, Q., & Xu, J. Y. (2007). Wavelet analysis of the quasi-27d oscillations of solar index F10. 7. Chinese Astronomy and Astrophysics, 31(4), 400-409.

MacQueen, R. M., Eddy, J. A., Gosling, J. T., Hildner, E., Munro, R. H., Newkirk Jr, G. A., ... & Ross, C. L. (1974). The outer solar corona as observed from Skylab: Preliminary results. The Astrophysical Journal, 187, L85.

Mannucci, A. J., Wilson, B. D., Yuan, D. N., Ho, C. H., Lindqwister, U. J., & Runge, T. F. (1998). A global mapping technique for GPS-derived ionospheric total electron content measurements. Radio science, 33(3), 565-582.

McNamara, L. F. (1991). The ionosphere: communications, surveillance, and direction finding. Krieger publishing company.

Meggs, R. W., Mitchell, C. N., & Howells, V. S. C. (2005, March). Simultaneous observations of the main trough using GPS imaging and the EISCAT radar. In Annales Geophysicae (Vol. 23, No. 3, pp. 753-757). Copernicus GmbH.

Miller, A. (1979). Elements of meteorology (No. 551.5 M54 1979).

Moldwin, M. (2008). An introduction to space weather (Vol. 1). Cambridge: Cambridge University Press.

Mstl, C., Rollett, T., Frahm, R. A., Liu, Y. D., Long, D. M., Colaninno, R. C., ... & Vrnak, B. (2015). Strong coronal channelling and interplanetary evolution of a solar storm up to Earth and Mars. Nature Communications, 6(1), 1-10.

Nahavandchi, H., & Soltanpour, A. (2008). Local ionospheric modelling of GPS code and carrier phase observations. Survey Review, 40(309), 271-284.

Nava, B., Coisson, P., & Radicella, S. M. (2008). A new version of the NeQuick ionosphere electron density model. Journal of Atmospheric and Solar-Terrestrial Physics, 70(15), 1856-1862.

Ngwira, C. M., McKinnell, L. A., Cilliers, P. J.,& Coster, A. J. (2012). Ionospheric observations during the geomagnetic storm events on 2427 July 2004: Longduration positive storm effects. Journal of Geophysical Research: Space Physics, 117(A9).

Okoh, D., McKinnell, L. A., Cilliers, P., Okere, B., Okonkwo, C., & Rabiu, B. (2015). IRI-vTEC versus GPS-vTEC for Nigerian SCINDA GPS stations. Advances in Space Research, 55(8), 1941-1947.

Olwendo, O. J., & Cesaroni, C. (2016). Validation of NeQuick 2 model over the Kenyan region through data ingestion and the model application in ionospheric studies. Journal of Atmospheric and Solar-Terrestrial Physics, 145, 143-153.

Parker, E. N. (1965). Dynamical theory of the solar wind. Space Science Reviews, 4(5-6), 666-708.

Pesnell, W. D. (2016). Predictions of solar cycle 24: How are we doing?. Space Weather, 14(1), 10-21.

Prlss, G. W. (2004). Absorption and dissipation of solar wind energy. In Physics of the Earths Space Environment (pp. 349-399). Springer, Berlin, Heidelberg.

Prlss, G. W. (2005). Space weather effects in the upper atmosphere: Low and middle latitudes. In Space Weather (pp. 193-214). Springer, Berlin, Heidelberg.

Prlss, G. W. (2006). Ionospheric F-region storms: unsolved problems. BONN UNIV (GERMANY FR).

Pulkkinen, T. (2007). Space weather: terrestrial perspective. Living Reviews in Solar Physics, 4(1), 1-60.

Rama Rao, P. V. S., Gopi Krishna, S., Niranjan, K., & Prasad, D. S. V. V. D. (2006, December). Temporal and spatial variations in TEC using simultaneous measurements from the Indian GPS network of receivers during the low solar activity period of 20042005. In Annales Geophysicae (Vol. 24, No. 12, pp. 3279-3292). Copernicus GmbH.

Ratcliffe, J. A. (1974). The formation of the ionosphere. ideas of the early years (19251955). Journal of Atmospheric and Terrestrial Physics, 36(12), 2167-2181.

Rees, M. H. (1989). Physics and chemistry of the upper atmosphere. Cambridge University Press.

Rishbeth, H., & Garriott, O. K. (1969). Introduction to ionospheric physics. Introduction to ionospheric physics.

Rishbeth, H., & Van Eyken, A. P. (1993). EISCAT: early history and the first ten years of operation. Journal of atmospheric and terrestrial physics, 55(4-5), 525-542.

Romero, L. M. (2002). Seasonal changes in plasma glucocorticoid concentrations in free-living vertebrates. General and comparative endocrinology, 128(1), 1-24.

Schunk, R., & Nagy, A. (2009). Ionospheres: physics, plasma physics, and chemistry. Cambridge university press.

Schwabe, H. (1844). Sonnenbeobachtungen im Jahre 1843. Von Herrn Hofrath Schwabe in Dessau. Astronomische Nachrichten, 21, 233.

Schwenn, R., Lago, A. D., Huttunen, E., & Gonzalez, W. D. (2005, March). The association of coronal mass ejections with their effects near the Earth. In Annales Geophysicae (Vol. 23, No. 3, pp. 1033-1059). Copernicus GmbH.

Solanki, S. K., Inhester, B., & Schssler, M. (2006). The solar magnetic field. Reports on Progress in Physics, 69(3), 563.

Solanki, S. K., Krivova, N. A., & Haigh, J. D. (2013). Solar ir radiance variability and climate. Annual Review of Astronomy and Astrophysics, 51, 311-351.

Svalgaard, L., Cliver, E. W., & Le Sager, P. (2004). IHV: a new long-term geomagnetic index. Advances in Space Research, 34(2), 436-439.

Szuszczewicz, E. P., Blanchard, P., Wilkinson, P., Crowley, G., FullerRowell, T., Richards, P., ... & Zolesi, B. (1998). The first realtime worldwide ionospheric predictions network: An advance in support of spaceborne experimentation, online model validation, and space weather. Geophysical research letters, 25(4), 449-452.

Tariku, Y. A. (2019). Assessment of improvement of the IRI model over Ethiopia for the modeling of the variability of TEC during the period 20132016. Advances in Space Research, 63(5), 1634-1645.

Thernisien, A., Vourlidas, A., & Howard, R. A. (2011). CME reconstruction: pre-STEREO and STEREO era. Journal of Atmospheric and Solar-Terrestrial Physics, 73(10), 1156-1165.

Tinsley, B. A., & Yu, F. (2003). Atmospheric ionization and clouds as links between solar activity and climate. GEOPHYSICAL MONOGRAPH-AMERICAN GEOPHYSICAL UNION., 141, 321-340.

Tsagouri, I., Belehaki, A., Moraitis, G., & Mavromichalaki, H. (2000). Positive and negative ionospheric disturbances at middle latitudes during geomagnetic storms. Geophysical Research Letters, 27(21), 3579-3582.

Tsuneta, S., Hara, H., Shimizu, T., Acton, L. W., Strong, K. T., Hudson, H. S., & Ogawara, Y. (1992). Observation of a solar flare at the limb with the YOHKOH Soft X-ray Telescope. Publications of the Astronomical Society of Japan, 44, L63-L69.

Van Melle, M. J. (1995, December). Cesium and rubidium frequency standards status and performance on the GPS program. In Proceedings of the 27th Annual Precise Time and Time Interval Systems and Applications Meeting (pp. 167-180).

Wallace, J. M., & Hobbs, P. V. (1977). Atmosphere science-an introductory survey. Atmosphere science-an introductory survey, V.

Webb, D. F., & Howard, R. A. (1994). The solar cycle variation of coronal mass ejections and the solar wind mass flux. Journal of Geophysical Research: Space Physics, 99(A3), 4201-4220.

Yu, Y., WAN, W. X., LIU, L. B., & ZHAO, B. Q. (2009). A global ionospheric TEC perturbation index. Chinese Journal of Geophysics, 52(5), 907-912.

Zhao, B., Wan, W., Liu, L., Yue, X., & Venkatraman, S. (2005, December). Statistical characteristics of the total ion density in the topside ionosphere during the period 1996-2004 using empirical orthogonal function (EOF) analysis. In Annales Geophysicae (Vol. 23, No. 12, pp. 3615-3631). Copernicus GmbH.

Zolesi, B., & Cander, L. R. (2014). The General Structure of the Ionosphere. In Ionospheric Prediction and Forecasting (pp. 11-48). Springer, Berlin, Heidelberg.

Declaration

I hereby declare that this thesis is my original work and has not been presented for a degree in any other university, and that all sources of materials have been duly acknowledged.

Name: Kasech Gezahegn

Signature: ——————————

Date: ——————————

This thesis has been submitted for examination with my approval as a University advisor.

Name: Dr. Tsegaye Kassa

Signature: ——————————

Date: ——————————-